AD-A019 710

ANALYSIS OF AEROSOL TRANSPORT

Reinhold Reiter, et al

Fraunhofer-Gesellschaft, Garmisch-Partenkirchen

Prepared for:

Army Research and Development Group (Europe)

July 1975

AD _____

ANALYSIS OF AEROSOL TRANSPORT

FINAL TECHNICAL REPORT

BY

Reinhold Reiter

Walter Carnuth

Michael Littfass

and

N. C. Varshneya *)

July 1975

EUROPEAN RESEARCH OFFICE
United States Army
London England

Grant Agreement No. DA-ERO-591-73-G0057

Institut für Atmosphärische Umweltforschung
der Fraunhofer-Gesellschaft

D-8100 Garmisch-Partenkirchen, Germany
Kreuzeckbahnstraße 19

*) Univ. of Roorkee, India

UNCLASSIFIED

SECURITY CLASSIFICATION OF THIS PAGE (When Data Entered)

REPORT DOCUMENTATION PAGE		READ INSTRUCTIONS BEFORE COMPLETING FORM
1. REPORT NUMBER	2. GOVT ACCESSION NO.	3. RECIPIENT'S CATALOG NUMBER
4. TITLE (and Subtitle) Analysis of Aerosol Transport		5. TYPE OF REPORT & PERIOD COVERED Final Technical Report July 1975 July 1975 6. PERFORMING ORG. REPORT NUMBER
7. AUTHOR(s)		8. CONTRACT OR GRANT NUMBER(s) Grant No. DA-ERO-591-73 -G0057
9. PERFORMING ORGANIZATION NAME AND ADDRESS Institut für Atmospharische Umwelfforsch- der Fraunhofer-Gesellschaft ung D-8100 Garmisch-Partenkirchen, Germany		10. PROGRAM ELEMENT, PROJECT, TASK AREA & WORK UNIT NUMBERS IT161102BH57-01
11. CONTROLLING OFFICE NAME AND ADDRESS USA R&D GP (EUR) BOX 15, N.Y. NEW YORK 09510		12. REPORT DATE July 1975 13. NUMBER OF PAGES ~~80~~ 93
14. MONITORING AGENCY NAME & ADDRESS(if different from Controlling Office)		15. SECURITY CLASS. (of this report) Unclassified 15a. DECLASSIFICATION/DOWNGRADING SCHEDULE

16. DISTRIBUTION STATEMENT (of this Report)

Approved for Public Release; Distribution Unlimited

17. DISTRIBUTION STATEMENT (of the abstract entered in Block 20, if different from Report)

18. SUPPLEMENTARY NOTES

19. KEY WORDS (Continue on reverse side if necessary and identify by block number)

Aerosol transport; Lidar System; Photon; telemetry

20. ABSTRACT (Continue on reverse side if necessary and identify by block number)

Report presents a detailed description of the recently installed, and currently functioning, lidar system, including data acquisition and processing. Extensive mathematical and theoretical procedures have been worked out for calibration of the system, using simultaneously acquired aerosol and aerological data, and for evaluation of the return signals once the system is absolutely calibrated. The procedures are described in detail, examples of calibration measurements are presented and discussed.

DD FORM 1 JAN 73 1473 EDITION OF 1 NOV 65 IS OBSOLETE

UNCLASSIFIED

SECURITY CLASSIFICATION OF THIS PAGE (When Data Entered)

AD _____

ANALYSIS OF AEROSOL TRANSPORT

FINAL TECHNICAL REPORT

BY

Reinhold Reiter

Walter Carnuth

Michael Littfaß

and

N. C. Varshneya *)

July 1975

EUROPEAN RESEARCH OFFICE
United States Army
London England

Grant Agreement No. DA-ERO-591-73-G0057

Institut für Atmosphärische Umweltforschung
der Fraunhofer-Gesellschaft

D-8100 Garmisch-Partenkirchen, Germany
Kreuzeckbahnstraße 19

*) Univ. of Roorkee, India

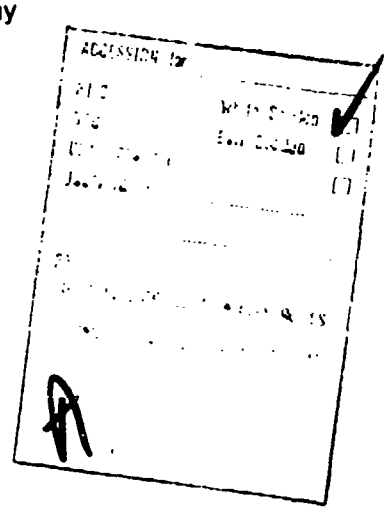

Table of contents

page

ABSTRACT

The lidar system may now be considered as being essentially completed. A detailed description in its present, final state, including data acquisition and processing, is given. Most recent extensions of the system are photon counting with range gating facilities, as well as electromechanical fluorescence suppression, which both provide a considerable increase in sensitivity for long-range, stratospheric aerosol sensing up to more than 30 km altitude. Examples of all modes of data recording including photon counting are presented. Furthermore, examples of simultaneous lidar backscatter measurements and cable-car recordings of profiles of Aitken nuclei concentration and aerological parameters are discussed. A first high-altitude measurement using the photon counting method is presented.

Extensive mathematical and theoretical procedures have been worked out for calibration of the system, using simultaneously acquired aerosol and aerological data, and for evaluation of the return signals once the system is absolutely calibrated. The procedures are described in detail, examples of calibration measurements are presented and discussed.

I. OBJECTIVES AND BACKGROUND

1. Preliminary Remarks

The present report subsequently continues and extends information given in the preceding Annual Report of June 1974 (1) under the same grant (DA-ERO-591-73-G0057). In order to avoid repetition, reference with regard to the General Background is made to (1).

2. Main Objective of Work in Reporting Period

The objective of our work under above grant is to develop a calibrated lidar system for aerosol remote sensing, and to employ it for studying aerosol transport, especially for monitoring the vertical aerosol distribution as function of aerological parameters.

The course our efforts took to develop the lidar system as such, as well as to establish the necessary theoretical basis for utilizing data obtained, has revealed that considerable work will yet have to be expended to attain the objective set. We therefore considered it expedient during the reporting period to concentrate our resources on largely completing two branches of our basic development work:

a) technological development of the lidar system and of the requisite electronic data processing system;
b) establishing the theoretical basis and computer programs for numeric evaluation of the recorded data.

By contrast, the performance of series of actual measurements has been temporarily postponed. We have limited our work to collecting lidar data, aerosol parameters obtained at our stations and by the cable-car telemetry system,

and aerological data on single days of especially favorable atmospheric conditions, to make available some material for the initial testing of the developed lidar calibration method.

Detailed reports on the above items (1) and (2) are found in the chapters below. The functioning of the lidar system at its final stage of completion, and of the evaluating system, is represented in some examples. Likewise the lidar calibration method developed by us, is presented by some numerical examples.

Completion of lidar calibration as well as practical employment of the entire system for aerosol remote sensing are intended to be accomplished in the scope of the next grant.

II. OBTAINING OF DATA JULY 1974 - JUNE 1975

Those facilities of our Institute that are essential within the scope of the grant, were employed partly to run continuous measurements, partly to conduct series of measurements or single measurements, the extent of which is briefly summarized as follows.

1. Rawinsonde

A total of 22 ascents with an average summit height of 30 km, were conducted and evaluated, partly for purposes of lidar calibration, partly within the scope of basic atmospheric investigations.

2. Cable Car Telemetry Data

A total of 1441 measuring runs were conducted by the Zugspitze cable-car telemetry system in the reporting period,

and were largely evaluated. The aerological data, and profiles of aerosol concentration (Aitken nuclei) were used, in part, for comparison against the lidar backscattering profiles.

3. Measurements Taken at Three Stations

Following measurements and recordings have been continued without any interruptions:

a) Natural radioactivity in the air (RaB, RaC);
b) Condensation nuclei with size distribution;
c) Impactor measurements;
d) Atmospheric electricity;
e) Meteorology.

4. Lidar Backscattering Profiles

The extent of the lidar backscattering profiles taken is as follows:
For purposes of lidar calibration, synchronous measurements were conducted by lidar, rawinsonde and impactors, on 12 days.

III. FINAL TECHNICAL STATUS OF THE LIDAR SYSTEM, INCLUDING DATA PROCESSING

The lidar system, which had been put into operation in 1973, had been described in its basic version in the 5th annual report. During the following two years the system had been extended by a number of supplementary facilities. Now it may be considered as completed and shall be described as a whole in detail. The mechanical layout of the system is shown in Fig.III.1, the block scheme Fig.III.2 shows the electronics in detail.

1. Laser Transmitter with Power Supply (cf. Figs III.1 and III.2)

The Q-switched ruby laser transmitter (1) is mounted horizontally on a vibration-free frame (2) within a penthouse on the roof of the Institute building.
The holographic quality, Czochralski type ruby (length 165 mm, diameter 9.5 mm) is installed in a solid metal block (3) with an elliptical, silver coated cavity, together with the flash lamp, and is water-cooled. The resonator of approximately 1.500 mm length consists of a highly reflecting end mirror in the rear (4) and a front output mirror (5) (BK7 glass plate, 16% reflection). Filtered and dried air from an Institute-own compressed-air system is blown on the ruby end faces to protect them, particularly from condensed water. Q-switching is done by a Kerr cell (6) and a polarizer (7).

The output power is 100 Megawatts maximum, the pulse length about 20 nanoseconds. This results in a pulse energy of 2 Joules. The beam divergence is 3 mrad total (no expanding telescope is used).

Behind the end mirror, a battery-operated trigger sensor (8) is mounted, which picks up the residual laser light penetrating the mirror by means of a photodiode, and generates a trigger pulse for the data acquisition electronics.

The power supply for the flashlamp, (9), which includes the Kerr cell driving unit (10) are located in the same room. It is amply designed for permitting a pulse repetition frequency of up to 2 sec^{-1} at the full output energy of 4 kilowattseconds per pulse. This is of great benefit in observing rapidly changing processes. For stability reasons, however, the repetition frequency is to

be limited to 1 sec^{-1}. Through an aperture in the wall of the room, the laser beam hits a 45 deg. mirror and is directed upwards (see below).

2. Frequency Doubler

A KD*P crystal (11) is used for generating the doubled ruby frequency, 347 nanometers. A filter cuvette (12) containing copper sulphate solution removes the residual undoubled laser light. Both crystal and cuvette are mounted, together with one 45 degree dielectric first surface mirror (13) for each transmitter frequency, on a carriage (14) just above the receiving telescope secondary mirror (described later). By means of a servo motor operated from the operating console (15) the carriage can be moved from one position to the other, thus swinging the doubling equipment into and out of the laser beam path and properly positioning either deviating mirror. Since the doubling efficiency of the KD*P crystal (about 8% maximum) depends very critically on the exact positioning of its optical axis with respect to the laser beam (index matching), it is alignable by two precision screws. The switching time is about 20 seconds, allowing double frequency firings within short time intervals.

3. Receiver Unit

3.1. Telescope

The backscattered laser light is picked up by an astronomical quality, 52 cm dia. Cassegrain reflecting telescope (16), consisting of a concave primary mirror (17) with a borehole in its center and a convex secondary mirror (18) generating a secondary focus just behind the borehole. The resulting equivalent focal length is 3.8 m. The telescope is mounted in a fixed vertical position within a barrel-shaped waterproof case (19) permanently installed in the open on the observation platform. It is

closed on top by a tilted precision quartz glass plate allowing rain and snow water to flow off easily, with the transmitter exit window (20) placed horizontally in its middle. This window also consists of quartz glass providing good transmission for the 347 nm wavelength.

The laser beam enters horizontally through a lateral flange and hits the deviating mirror/frequency doubler assembly mentioned above, and leaves the case through the exit window. Despite some disadvantages, e.g. stray light generation in the case, we chose this concentric configuration to be able to receive returns from all ranges of interest without any readjusting.

A temperature regulated heating prevents water condensate formation and keeps the temperature of the frequency doubling crystal constant. This is necessary because the optimal position of the crystal depends on temperature.

Within the focal plane of the telescope an iris stop (21) limiting the field of view of the system, and an optical shutter (22) operated electrically from the console are mounted. Below the shutter, a filter turret (23) containing a 694 and a 347 nm interference filter, bandwith 3 nm, for background reduction, and a gray wedge (24) are placed. Both units are also operated from the console by magslips. By means of the gray wedge, the sensitivity of the receiver can be reduced if necessary.

3.2. Photomultiplier Tube Assembly

The signals are received by an EMI 9816 photomultiplier tube (PMT) with S 20 cathode (25), which is located inside a commercial cooling box (26). In order to reduce the dark current the PMT can be cooled down to minus 20 deg. by means of Peltier elements. The light enters

the cooling box through a double-walled, heated quartz window (27) which is evacuated to prevent condensate formation. Outside the cooling box a collimating lens (28) and a holder for a polarizer (29) is installed. By means of the polarizer the degree of polarization of the backscattered light can be measured. For this purpose the box is mounted on a rotatable support with a vernier scale (30). With the onset of double frequency operation polarization measurements have become more difficult since the polarization planes of the 694 nm and 347 nm laser beams are normal to each other.
Finally, the PMT box can be aligned with respect to the optical axis of the telescope by a precision X-Y-adjust. The coil (31), which is attached to the photomultiplier tube, effects the gain of the tube as mentioned later. The operating voltage for the PMT is supplied by a highly stabilized Ortec high voltage power supply (32). The output signal is fed to the data acquisition electronics via a 50 Ohms terminated cable.

3.3. t^2-Control

Due to its decrease with the square of distance, the return signal traverses a very wide amplitude range which the photomultiplier tube and data acquisition have to cope with. In extreme situations, especially when the scattering function itself grossly decreases with altitude, the PMT may be overloaded by the strong nearby signal and, nevertheless, the faint returns from greater distances hardly to be measured. For this reason a device had been provided with the initial version of the lidar system which permits controlling the gain of the PMT proportionally to the square of the time elapsed from the releasing of the Q-switch pulse. This is done by applying a variable magnetic field via the coil (31) to the PMT. By this field the secondary electrons are more or less

strongly deflected from the dynodes and so the gain is reduced. The current through the coil is generated in the control unit (33) and varies by a definite time function which was empirically established so as to result in a photomultiplier gain increasing with the square of time. Thus the distance dependence of the return signal is eliminated.

Since this magnetic PMT gain control is well operating only over a gain range of about 2.5 powers of ten, the time range of the device is also limited. In view of our intention to measure at higher levels of altitude, the time range was fixed to range from 13 to 226 microseconds, corresponding to an altitude range from 2 to 40 km.

Triggered by a reference pulse generated in time with the flash-lamp ignition, about 1 ms prior to the Q-switch pulse, the coil current goes to its maximum value, or the gain to its minimum, and remains then constant until 13 µsec after releasing of the Q-switch pulse. Then the gain increases with the square of time and remains constant again, 226 µsec after Q-switching, at its maximum value.

Controlling amplification directly on the photomultiplier tube as opposed to a succeeding electronic system, in addition to simplifying evaluation of the analog signal, offers the advantage that an overloading of the PMT by the sometimes very intense close-range signal is prevented. Of course, the constant skylight background is also increased as to interfere with the measuring signal, so we can work with the t^2-control only at night.

4. Calibration of Transmitter and Receiver

In order to be able to compare lidar measurements among

each other and also against other date it is necessary to normalize the unit. This applies especially to two-frequency operation. The energy of each individual laser pulse, both 694 and 347 nm, is to be measured, therefore, or monitored. For this purpose, a small amount of the laser pulse, reflected back from the output window (20), is fed to two photodiodes (34) via a quartz fiber optics system (35). By suitable filters, it is ensured that one of the diodes is sensitive only to red (694 nm) light, the other one to ultraviolet (347 nm) light. By this reason only one common output line is necessary (36).
A 50 megahertz A-D converter gives a 4 bit digital reading of the pulse amplitude.
Both diodes are calibrated by simultaneous calorimeter measurements. Besides a conventional calorimeter with sheet copper measuring and reference cones, a new volume absorbing calorimeter is now available. The laser energy is absorbed in a special color glass plate, which avoids the uncontrollable reflection losses of the copper cones. Also recalibration is much easier due to a special calibration coil. The calorimeter is calibrated by letting a well-defined amount of electric energy flow for a short time through this coil.
Since it is necessary to measure the laser pulse energy at a certain minimum distance from the output window (20) to avoid additional reflection back to the photodiodes, a preadjusted mount has been constructed to for fastening the calorimeter in the proper position above the laser beam exit window (37).
Figs III.3 and III.4 show the calibration curves for both photodiodes. The curves are linear but show a considerable zero-point offset. This actually increases the accuracy of the digital photodiode readings beyond the 4-bit resolution limit.
Absolute calibration of the receiver is very difficult. Usually, lidar receivers are calibrated relatively with

respect to the transmitter pulse power using return signals from an atmosphere with known backscatter function. This procedure is described in detail in section V of this report.

For checking the linearity or possible gain changes of the photomultiplier tube, a precision microsecond flashlamp is available. This flashlamp may be triggered with variable delay, and so it is suitable also for checking the performance of the t^2-control unit.

5. Data Acquisition

The return signals may now be recorded in three different ways:

a) analog recording by means of oscilloscope and camera,
b) digital recording by means of transient recorder, and
c) single photon counting with range gating.

5.1. Analog Recording

During the first year of operation of the lidar system, only analog data recording was possible. The signals delivered by the PMT are fed to a dual beam Tektronix 556 (38) oscilloscope. The traces on the CRT are photographed either on 4 x 5" Polaroid film or 70 mm perforated negative film. Evaluation has to be done manually in this case. Fig.III.5 shows a Polaroid print with examples of return signals photographed directly from the oscilloscope screen.

5.2. Digital Recording with Punch Tape Data Output

For digitization and storage of the data a transient re-

corder type Biomation 8100 (39) is provided. This recorder contains a very rapid (100 MHz) A-D converter with 8 bit (=.4%) amplitude resolution. The memory capacity is 2048 words à 8 bit. The minimum sample interval is 10 nanoseconds, which results in an altitude resolution of 1.5 m. The transient recorder is triggered in a manner very similar to an oscilloscope. In our case it is triggered externally by the trigger sensor (8). Dual time base operation allows recording of the "upper" part of the return signal with a slower sampling rate and thus obtaining the exact amplitude zero point, which depends on the varying sky background.

The stored data may be output in three different ways. On the one hand, a reconstructed analog signal output is provided in two forms. The Y display output presents this analog signal repetitively to permit the signal to be continuously displayed on a CRT display or oscilloscope. For this purpose, a suitable X output is also provided. The reconstructed analog signal is also available for output to a strip-chart recorder or Y-T plotter (we are using a Brush-type rapid strip-chart recorder (40) for this purpose, see Figs III.8 - III.11). The plot time is 20 seconds.

Finally, via a digital output the stored digital data may be read, at reduced speed, directly into a computer in online operation, or may be transferred via interface on magnetic or punch tape, or the like. In our case, data output is done in binary form on 8-channel punch tape via an interface (41) and a Facit tape punch (42). For further processing the punch tape is read into our computer where the data are normalized with respect to transmitter output power and receiver sensitivity (e.g. PMT high voltage setting), and range corrected by multiplying with the square of distance. Then the converted (and smoothed, if necessary) signal is plotted on a high-

speed incremental plotter.

Due to the R^2-law the return signal covers a wide range of amplitude. As a consequence only signals from an altitude range not exceeding 2 km can be processed by the transient recorder without a considerable loss in resolution. For this reason a gain-switching amplifier (43) is available, which actually consists of two amplifiers with gains of 2.65 and 29.3, respectively, operating in parallel. A special electronic circuitry switches very rapidly from one amplifier output to the other. During steady state conditions, the low gain amplifier is running. When a laser pulse is initiated, a trigger signal from one of the photodiodes is received and a delay time generator started. At the end of the presettable time delay, the output is switched to the high gain amplifier, and then back again after 5 milliseconds. The switching is very rapid, so that only a few data words in the transient recorder are lost.

5.3. Examples of Data Records

Figs III.5 - III.12 show examples for the different types of data recording and plotting.
Fig.III.5 is a Polaroid photograph of original lidar returns as displayed on the oscilloscope screen. The time or altitude axis points up. The rotatable, indexed sliding back of the camera allows recording multiple images on one photo. In Fig.III.5 five backscatter signals are recorded with different oscilloscope gain and sweep settings. Beginning with the left, they are the following:

Signal No.1: 5 mV/div., 10 µsec/div. = 1500 meters/div.,
" " 2: 5 mV/div., 5 µsec/div. = 750 meters/div.,
" " 3: 5 mV/div., 2 µsec/div. = 300 meters/div.,
" " 4: 20 mV/div., 2 µsec/div. = 300 meters/div.,
" " 5: 100 mV/div., 2 µsec/div. = 300 meters/div.,

All signals are 694 nm returns. An aerosol layer with an upper boundary at 2500 m above station level (3250 m above sea level) is clearly to be recognized, with some fine structure below.
It is obvious that the manual evaluation of the data, using only the oscilloscope photos, is a tedious and time-consuming task. The Polaroid photo Fig.III.6 represents three pairs of simultaneous 694 and 347 nm return signals as recorded with the Biomation 8100 transient recorder. The reconstructed analog signals were displayed on the CRT screen of the oscilloscope and photographed, each pair of signals with coincident coordinate axes. The smaller signals are the 347 nm (ultraviolet) signals. The T-axes point up, the scale is 2 µsec/div. or 300 m/div.. The red (694 nm) signals again show considerable fine structure due to aerosol inhomgenities. The peak at 500 m above station level in the 0930 CET signal may be generated by a transient small cloud. In contrary, in the ultraviolet (347 nm) signal the influence of aerosol is much less pronounced. This is a feature common to all ultraviolet returns and is surely caused by the much higher molecular part of the backscatter function at the 347 nm wavelength (see sections IV and V of this report).

Instead of taking photos, the reconstructed analog signal generated by the transient recorder may be recorded via an additional output connector by a fast Y-T strip chart recorder, as mentioned above. We are using a Brush 220 pressurized ink recorder. The total analog signal is output within 20 seconds. Using a chart speed of 5 mm/sec, this results in an overall signal length on the chart of 10 cm. Figs III.7 - III.10 are copies of original Brush strip charts, showing two pairs of double frequency return signals. In these cases, the gain-switching amplifier had been used. The gain switching is indicated by a very rapid increase in signal amplitude. The small peak just

below the switching point is an artefact generated by the switching circuitry and seems to be unavoidable. It is eliminated during computer processing of the digital data. Again the striking lack of fine structure of the 347 nm signals (besides the cloud peak at 2500 m a.s.l. in Fig.III.8), as compared to the 694 nm signals, is to be mentioned.

The "shoulder" in the 694 nm signal curve Fig.III.9 at 2500 m a.s.l. (denoted by an arrow), which indicates an aerosol layer, is hardly to be recognized in the corresponding 347 nm signal, Fig.III.10.

Fig.III.11 represents a pair of double frequency backscatter profiles. The original return signals are shown in the left part of Fig.III.6. The digitized signals had been output on punch tape and fed to the computer. Then they were normalized and range-corrected by multiplying with the square of distance, and plotted by our high-speed incremental plotter.

Due to the limited amplitude resolution of the transient recorder, the influence of digitization shows up very clearly in the upper parts of the plots, especially in the 347 nm profile. As mentioned above, these signals had been obtained before the gain-switching amplifier was available. This amplifier largely avoids the influence of resolution limitation.

5.4. Single Photon Counting

As mentioned above, the amplitude of the lidar return signals decreases rapidly with distance or altitude. Due to the limited quantum efficiency of the PMT cathode, beyond a certain minimum distance depending on transmitter power and receiver sensitivity, the signals are more and

more dissolved into individual photon peaks. In this case, the sensitivity and signal-to-noise ratio of the receiver is greatly increased by the range-dependent photon counting technique. In our case, a ten-channel photon counter is provided (44). By a special gating circuitry, the ten counters are "opened" in series one after the other, for a presettable gating time. The first channel is opened after an also presettable time delay after the laser pulse initiation. An eleventh channel, opened 1 millisecond after the 10th, serves as reference channel for background measurement.

Two modes of operation are possible with the counter. In the one (single shot) mode, the stored photon counts are output automatically after each laser shot on punch tape in BCD code. In the other mode ("adder" mode), counts generated by a presettable number of laser shots are stored in two additional storage registers. In detail, the process is the following: with n denoting the preset number of single shot counts to be added, during the first n shots, the counts of channel 1 and 2 are added in the two storage registers. Then the content of the registers is output automatically on punch tape, and the registers are reset. Subsequently, during the next n shots, the counts of channel 3 and 4 are added in the same way in the two registers, given out on tape, and so on until the channel 9 and 10 counts are added and output on the punch tape. This completes the whole cycle.

In order to get single photon pulses with sufficient amplitudes for photon counting (some ten millivolts) at the anode of the photomultiplier tube, the tube has to be operated with relativley high voltage (about 2.2 kilovolts in our case). This would imply a heavy overload of the tube by the strong short-range signal. For this reason, a range gating facility is provided with the pho-

ton counter. In this mode of operation, dynode 7 of the photomultiplier is kept at a voltage which results in a nearly zero overall gain of the tube. Only during the gate interval when the counters are "open", this voltage is changed to its normal value by means of an appropriate electronic circuitry.
The range gating facility may be useful also for analog signal recording, e.g. when signals from higher altitudes are to be recorded with good resolution.

6. Fluorescence Suppression

In addition to the coherent laser light the ruby also emits incoherent fluorescent light for about one millisecond. Although it is more divergent and much less intensive than the laser pulse, this fluorescence would under unfavorable conditions (strong short-range backscatter) superpose the faint return signals from high altitudes. For this reason a mechanical chopper (45) is provided which blocks the beam path completely 137 µsec after Q-switching which corresponds to an altitude of 21 km. The chopper consists of a cylinder with two opposite holes and rotates with 200 r.p.s. An appropriate electronic control (46) with optical sensors ensures exact synchronization of chopper passage and Q-switch triggering.

7. A First Example for High Altitude Lidar Measurement

After final completion of the photon counting equipment, the weather conditions had been favorable for night-time high altitude lidar measurements for the first time on July 28, 1975.
At first, a series of 694 nm analog signals were recorded with the Biomation transient recorder using the range gating. The gate delay, i.e. the time lag between Q-switching and the beginning of the gate interval, had been

set to successively increasing values of 60, 80, 100, ..., 300 microseconds, corresponding to altitudes of 9 to 45 km above station level (9.75 to 45.75 km above sea level). The length of the gate interval itself was 30 µsec or 4.5 km. This resulted in a set of overlapping partial signals, which are shown as original strip chart plots in Fig.III.12. The surprisingly high amplitude of the signals, which by far exceeds the time resolution limit of the photon counter, clearly shows up in the diagram. Even from more than 70 km altitude a signal with non-zero amplitude is received, as shown in the upper right corner of Fig. III.12.

The partial signals, although very noisy, can be combined to a complete return signal, Fig.III.13. The signal amplitude decreases steadily with altitude, but as a range-correction clearly shows, too slowly. The backscatter cross section should decrease with altitude approximately proportional to the density of the atmosphere (the density of the standard atmosphere decreases from .4 kg/m^3 at 10 km a.s.l. to 3.7×10^{-3} kg/m^3 at 40 km).

Obviously a nearly constant background is superimposed to the measuring signal. This background was not generated by residual skylight, as test measurements demonstrated. It must be assumed, therefore, that the background is caused by ruby fluorescence. Since lidar returns from 30 km altitude showed no significant difference with and without using the fluorescence suppression, (cf. Fig.III. 17), it had not been used during the measurements described now. The first experiences seem to suggest, however, that it is not recommended at all to perform lidar measurements without fluorescence rejection, even under apparently favorable conditions.

If the probable fluorescence background, which actually doesn't need to be exactly constant, is subtracted from the signal, range-correction (i.e. multiplication with

the square of distance) results in the backscatter profile shown in Fig.III.14. Because if the poor signal resolution due to inherent noise, its fine structure cannot be considered to be real.
For single photon counting the signal amplitude is to be reduced considerably. For this purpose we shifted the gray wedge from the 100% to a 3.4% transmissivity position. Then again a series of shots was fired with the same set of range gate positions as described above. For reducing the statistical error ten shots were fired per range gate position and output on punch tape. It is to be borne in mind that the total gate interval, in our case 30 µsec or 4.5 km, is divided by the ten counting channels into ten parts of equal length. This results in an altitude resolution of 450 m.

A preliminary examination of the results showed a significant increase of the counts from channel 1 to about channel 4 or 5, independent of the gate delay setting. A somewhat lower count rate of the first channel might be due to a non-zero relaxation time for the gain of the photomultiplier tube to reach its final value after the beginning of the gate interval. A careful examination of the rise of the PMT current after "opening" of the range gate, when the tube is exposed to a constant light source (e.g. to the sky background), however, leads to the conclusion that this relaxation time doesn't exceed a few hundred nanoseconds. This results in a count reduction of the first channel by only a few percent. All other channels should show no differences in count rate at all, when a constant photon flux is fed to the PMT.

Maybe the mentioned differences are caused by improper alignment of the threshold of the photon counter input circuit. Otherwise, the channels have to be "calibrated" by counting photon pulses generated by a constant light

source (sky background).
In Fig.III.15 the counts of channels 2 to 10 have been added and thus the differences between the channels eliminated. Each series of counts is represented as an "I"-shaped bar. Its vertical extent denotes the length of the gate interval, the horizontal extent the statistical error, which is equal to the square root of the sum of the counts. The total counts per gate interval steadily decrease with altitude, but tend to approach a non-zero background in a similar manner as the analog signal, Fig.III.13. If this background is again subtracted and range-correction applied, the backscatter profile shown in Fig.III.16 is obtained. The meaning of the I's is the same as in Fig.III.15. Additionally, the density ρ of the standard atmosphere is plotted in the diagram in relative units. Obviously the backscatter profile doesn't fit to the density curve at mid-altitudes from about 20 to 40 km. This is surely not due to aerosol backscatter, but may rather be caused by a decrease of the fluorescence background. On the other hand, the step in the backscatter profile at 30 km altitude is might be possibly real.

These first high altitude lidar measurements showed, on the one hand, urgently that the rejection of the ruby fluorescence is much more important than it seemed to be previously. On the other hand, the extreme sensitivity of the photon counting method is to be emphasized, especially if the reduced receiver sensitivity due to the gray wedge is considered. By setting the gray wedge to a higher transmissivity position, a further increase of the measurement accuracy is possible at higher altitudes.

The high sensitivity of the photon counting method is very advantageous to 347 nm measurements, which are more limited in range due to the lower transmitter energy and

higher molecular extinction in that wavelength. For technical reasons, however, only 694 nm high altitude data are available up to now.

The measurements described above didn't show any aerosol backscatter with certainty. A night-time high altitude measurement performed in January 1975, before the installation of photon counting and fluorescence suppression, should be mentioned here, which revealed a very distinct backscatter peak at 20 km altitude, cf. Fig.III. 18. This peak is certainly due to an aerosol layer generated by the eruptions of the Fuego volcano (Guatemala) in October 1974. Conspicuous twilight phenomena had been additionally observed at that time during dusk and dawn.

IV. EMPIRICAL COMPARISONS OF LIDAR BACKSCATTER PROFILES WITH CABLE-CAR SONDE DATA

A few examples of empiric comparisons between lidar backscatter profiles, on the one hand, and results of cable-car soundigs, especially vertical profiles of Aitken nuclei number concentration, on the other, are presented below, see Figs IV.1 through IV.5.

In detail, the following parameters are measured by cable-car sondes:

a) Temperature (T),

b) Wet-bulb or psychrometer temperature (T'). This is the temperature of a ventilated, wet-tissue covered thermistor. It is the more below air temperature T, the drier the air, thus providing measure of relative humidity. Both temperature scales rise to the left.

c) Polar electric conductivities λ_+, λ_-. As mentioned

above, as a result of aerosol particles capturing small ions, conductivity will decrease with increasing particle number concentration. Thus, the purer the air, the greater the value of conductivity. Consideration must be given to the fact that high particle concentrations are measured with a lesser accuracy than low ones. Conductivity scales also rise to the left.

d) Aitken nuclei number concentration, N. A small Aitken nuclei counter provides total number of all particles per cc, above a limiting value of about .01 µm diameter which is determined by the expansion ratio, but otherwise irrespective of size distribution. Again, the scale rises to the left.

These profiles are compared against our lidar data which are represented by the variable $B = PZ^2/E$ (P = incident radiation power; Z = distance or altitude; E = transmitter pulse energy) in relative units, standardized, however, for each wavelength so as to be comparable among each other. As the lidar equation shows, term B or, respectively B_R for 694 nm wavelength, and B_{UV} for 347 nm, is proportional to the backscattering function, excepting extinction losses. Because of the short measuring distance in this case extinction is not assumed to have any considerable effect, at least in the red. Unlike all other parameters the B-scale in the graphs rises to the right.

In comparing B to N it must be considered that the backscattering function, unlike nuclei concentration, is a function of particle size distribution, roughly speaking in the form of preference to the large particles. Therefore, exact parallelism of the two parameters is not to be expected.

The profiles shown in Figs IV.1-5 were recorded 11 June 75 during a weather situation which is very typical of

a mountain valley opening into a plain: Due to heating of the mountain slopes by insolation in the hours of the forenoon air will ascend there. The resultant suction will cause air from the fore-plain which is more polluted and frequently also more humid, to be carried up the valley more and more. This process will stop toward the evening and be reversed in the course of the night. The flown-in air is replaced by air of a low aerosol content, flowing down from the slopes.

The Fig.IV.1 diagram, at 1020 CET, still shows an inversion at 2100 m a.s.l., well defined by temperature increase and humidity decrease, which had developed as a result of nocturnal radiation. Underneath we find, demonstrated by increased lidar backscatter and CN concentration plus decreased conductivity, a largely homogeneous well mixed layer of an aerosol content higher than that found above the inversion. The stop in lidar backscatter intensity is more distinct in the red (B_R) than in the ultraviolet (B_{UV}).

This situation observed quite frequently may be explained by the considerably higher molecular component of the backscattering function in the short wave range. Closely below the inversion a maximum is found in the B_R-curve, which is absent with the Aitken nuclei. However, it turns up again as minimum in the conductivity profile. This is assumed to be the phenomenon of precondensation. Within the range of the highest relative humidity marked by the shortest distance between T and T', the particles have absorbed water to such an extent that increased backscatter and capture of small ions have resulted. This interpretation is corroborated by the Fig.IV.2 diagram, which shows the conditions 20 minutes later. At the inversion single cumuli have already developed, one of which was temporarily located at the zenith

within the field of view of the receiver at time of the 694 nm lidar measurement causing a correspondingly intensive signal. Conductivities here show a very distinct minimum, while again no increased nuclei concentration is observed. With certainty the minimum of conductivity has been caused by the relatively fast capture of small ions on cloud droplets. Speed of capture of Aitken nuclei on cloud droplets is considerably slower, hence a similar effect is not observed.

Some time later, at 1413, the inversion has disintegrated between 2.1 and 2.2 km a.s.l., due to increasing turbulence. No structure whatsoever is found in lieu of it in any of the profiles. However, by the behavior of CN, λ_{+-}, B_R and B_{UV} air of high aerosol content having flown in from the foreplain can be detected in the lower layers. At its upper boundary, at 1450 m a.s.l., development of a new inversion has commenced. Different fine structures of CN and B_R may be caused by local conditions, inasmuch as we are here dealing with a dynamic process occurring in the horizontal (the distance between lidar and cable car sites is approximately 10 km).

About an hour later (1503 CET, Fig.IV.4) readily indicated by the behavior of lidar and cable-car data, the upper boundary of the air masses flowing up the valley has ascended to 1550 m a.s.l. and, like the temperature inversion at the same altitude, has become more distinct. Again half an hour later the upper aerosol boundary has arrived at 1750 m a.s.l. Below, the fine structure of B_R and CN has weakened. An interesting observation is the now existing minimum of particle concentration in the zone of inversion, becoming apparent in the CN and conductivity profiles, and judging from the absence of a corresponding minimum in the B_R profile is apparently limited to the small particles.

V. THE THEORETICAL BASIS OF LIDAR CALIBRATION

1. Introduction

Workers, such as COLLIS (1970), KATÉRLE (1970) and McCORMICK (1971), have demonstrated that it is posssible to obtain aerosol density profile in atmosphere using a two-frequency Ruby-laser, measuring the backward scattering received from different heights in the atmospheric column. They assumed the aerosol size to follow a Junge-distribution law:

$$n(D) = \frac{dn}{d(\ln D)} = \text{const. } D^{-\nu^*} \qquad (1)$$

and aerosol particles to have a real refractive index. Effect of humidity either on the size distribution or on refractive index was not considered.

The latest results on aerosol distribution by JUNGE and JAENICKE (1971) as well as the calculations of FOITZIK, SCHEITHAUER and SPÄNKUCH (1969) show that the aerosol size distribution can be profitably represented through an appropriate combination of log-normal distributions of the form:

$$n(D) = \frac{dn}{d(\ln D)} = \frac{N}{\sqrt{2\pi}\,s} \exp -\left(\frac{\ln \frac{D}{D_m}}{\sqrt{2}\,s} \right)^2 \qquad (2)$$

HÄNEL (1968, 1970 and 1972) has shown that humidity has effect on the size and refractive index of aerosol particles. This in turn affects the transmissivity as well as

the backscattering function for the transmitted and received lidar signals.

The purpose of this chapter is to describe a mathematical structure to be used for analyzing the signal data from a double-wavelength (0.6943 μ and 0.3472 μ) lidar stationed at Garmisch, with a purpose to obtain the density as well as the size distribution profile of aerosol in the atmosphere. The size distribution function of aerosol, at Garmisch, as obtained from actual measurements, has been assumed a bimodal log-normal function with the two maxima at $D_{m1} = 0.38$ μ and $D_{m2} = 2$ μ, and both the logarithmic standard deviations, $s_1 = s_2 = s = 0.3$ (Figs V.1a, b, c). The effect of humidity on size and refractive index has been duly taken into account and is summarized in Table V.1, and graphically represented in Fig.V.2, basing our calculation on the work of HÄNEL (1971).

Table V.1

Relative Humidity	$\frac{D}{D_o}$	Complex Refr. Index
0	1	1.62 - 0.0200 i
0.5	1.023	1.605 - 0.0187 i
0.7	1.070	1.570 - 0.0164 i
0.8	1.280	1.470 - 0.0097 i
0.85	1.400	1.420 - 0.0075 i
0.9	1.520	1.415 - 0.0058 i
0.92	1.585	1.405 - 0.0052 i
0.94	1.650	1.400 - 0.0045 i
0.96	1.84	1.380 - 0.0032 i
0.98	2.300	1.350 - 0.0015 i
1.00		1.330 - 0.0000 i

2. Basic Lidar Equations

The basic lidar equation for a backscatter signal, considering the scattering volume to be a point source located at altitude H, expressed as power incident on a coaxial receiver, is given by

$$W(\lambda,H) = \frac{1}{2}\, c\, Q(\lambda)\, \Sigma\, \frac{\tau^2(\lambda,\Delta H)}{H^2}\, F(180°,\lambda,H) \qquad (3)$$

After crossover of the laser pulse and receiver field of view the voltage at the oscilloscope follows from eq. (3) and is given by

$$V(\lambda,H) = Q(\lambda)\, A(\lambda)\, \frac{\tau^2(\lambda,\Delta H)}{H^2}\, F(\lambda,H) \qquad (4)$$

with

$$A(\lambda) = \frac{1}{2}\, c\, \Sigma\, R\, T(\lambda)\, S(\lambda) \qquad (4a)$$

If the oscilloscope voltage is normalized for the lidar output energy $Q(\lambda)$ and the square of height H^2, expressing it through a quantity

$$\frac{H^2\, V(\lambda,H)}{Q(\lambda)} = Y(\lambda,H)$$

then we can write

$$Y(\lambda,H) = \frac{H^2\, V(\lambda,H)}{Q(\lambda)} = A(\lambda)\, \tau^2(\lambda,\Delta H)\, F(\lambda,H) \qquad (5)$$

The quantities τ^2 and F are implicit functions of molecular and aerosol densities. Since we are considering the aerosol distribution as double-log-normal, we have two number densities - one for each distribution - $N_1(H)$ and $N_2(H)$. The total aerosol density, $N(H) = N_1(H) + N_2(H)$.

3. Evaluation of $F(\lambda,H)$

$F(\lambda,H)$ is the total scattering function, the sum of the molecular - and the aerosol-scattering functions:

$$F(\lambda,H) = f_M(\lambda,H) + f_A(\lambda,H) \tag{6}$$

For backscattering, $f_M(\lambda,H)$ is given by

$$f_M(\lambda,H) = \frac{9}{4\lambda^4} \frac{1}{N_M(H)} \left[\frac{m_M(H)^2-1}{m_M(H)^2+2}\right]^2 \cdot \frac{3(2+\Delta)}{6-7\Delta} \tag{7'}$$

where $\Delta = 0.0350$, for dry air, is the depolarization factor. With $m_M(H) \approx 1$, equation (7') approximates to

$$f_M(\lambda,H) = \frac{1.0608}{\lambda^4} \cdot \frac{(m_M(H)-1)^2}{N_M(H)} \tag{7}$$

From Rawinsonde values for pressure, temperature and humidity at different altitudes, the values of $m_M(H)$ (GOODY 1964) $N_m(H)$ and thereby $f_M(\lambda,H)$ can be calculated.

The aerosol backscattering function $f_A(\lambda,H)$ for a log-

normal distribution function dn(D) given by equation (2) is given by

$$\left.\begin{aligned} f_A(\lambda,H) = f_A(dn(D),\lambda,m_A(H)) &= \frac{\lambda^2}{4\pi^2}\int_{D=o}^{\infty} i(\alpha,m_A(H))\ dn(D) \\ &= \frac{\lambda^2}{4\pi^2}\, i_G(\alpha_m,m_A(H))\ N_A \\ &= \Phi_G\ N_A \end{aligned}\right\} \quad (8)$$

$$\text{with} \qquad \Phi_G = \frac{\lambda^2}{4\pi^2}\, i_G, \qquad \text{and} \qquad (8a)$$

$$i_G = \frac{1}{\sqrt{2\pi}\,s}\int_{\alpha=o}^{\infty} \frac{i(\alpha,m_A)}{\alpha}\ \exp-\left[\frac{\ln\frac{\alpha}{\alpha_m}}{\sqrt{2}\,s}\right]^2 d\alpha \qquad (8b)$$

$i_G(\alpha_m,m_A,s)$ for various α_m, s and m_A (corresponding to humidity, g) have been calculated and tabulated. Then, for a double-log-normal distribution

$$\begin{aligned} F(\lambda,H) = f_M(\lambda,H) &+ \Phi_{G1}(\alpha_{m1},\ s,\ m_A(H))\cdot N_1(H) \\ &+ \Phi_{G2}(\alpha_{m2},\ s,\ m_A(H))\cdot N_2(H) \end{aligned} \qquad (9')$$

Or, in an abbreviated form

$$F(\lambda,H) = f_M(\lambda,H) + \Phi_{G1}(\lambda,H)\cdot N_1(H) + \Phi_{G2}(\lambda,H)\cdot N_2(H) \qquad (9)$$

where Φ_{G1}, and Φ_{G2} can be calculated from the tabulated values of i_g according to equation (8a), and $f_m(\lambda,H)$ from (7).

4. Evaluation of $\tau^2(\lambda,\Delta H)$

$\tau^2(\lambda,\Delta H)$ for a given thickness ΔH of atmospheric layer, within which it is assumed that the molecular and aerosol number densities are constant, is given by

$$\tau^2(\lambda,\Delta H) = \exp - \left[2\left(\sigma_M(H) + \sigma_A(H)\right) \Delta H \right] \qquad (10)$$

$$\text{with} \quad \sigma_M(H) = \frac{8\pi}{3} f_M(H) = \frac{8.8869}{\lambda^4} \cdot \frac{[m_M(H)-1]^2}{N_M(H)}, \qquad (11)$$

and $\sigma_A(H)$ for a log-normal distribution given by

$$\left.\begin{aligned} \sigma_A(H) &= \frac{\pi}{4} \int_{D=0}^{\infty} D^2 K_E(\alpha, m_A)\, dn(D) \\ &= \frac{\lambda^2}{4\pi} \alpha_m^2 K_G N_A \\ &= d_G N_A \end{aligned}\right\} \qquad (12)$$

$$\text{with} \quad d_G = \frac{\lambda^2 \alpha_m^2}{4\pi} K_G \tag{12a}$$

$$\text{and} \quad K_G = \frac{1}{\sqrt{2\pi}\, s\, \alpha_m^2} \int_{\alpha=0}^{\infty} \alpha K_E(\alpha, m_A) \exp - \left[\frac{\ln \frac{\alpha}{\alpha_m}}{\sqrt{2}\, s}\right]^2 d\alpha \tag{12b}$$

d_G and K_G for various α_m, s and m_A (corresponding to humidity, g) have been calculated and tabulated. Then, for a double-log-normal distribution

$$\sigma_A(H) = d_{G1} \cdot N_1(H) + d_{G2} \cdot N_2(H) \tag{13}$$

and $\tau^2(\lambda, \Delta H)$ will be given by equation (10), with equations (11) - (13), represented as

$$\tau^2(\lambda, \Delta H) = \exp \left(-2 \left[\sigma_M(\lambda, H) + d_{G1}(\lambda, H) \cdot N_1(H) + d_{G2}(\lambda, H) \cdot N_2(H) \right] \Delta H \right) \tag{14}$$

5. Scheme of Calculations

Equation (5)

$$Y(\lambda, H) = A(\lambda)\, \tau^2(\lambda, \Delta H) \cdot F(\lambda, H) \tag{15}$$

is the basis of all further calculations. We devide the atmospheric column above lidar into layers of convenient

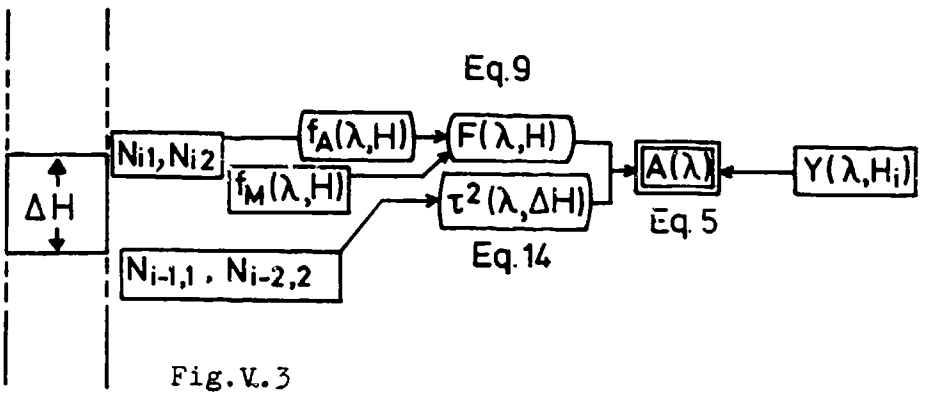

Fig. V. 3

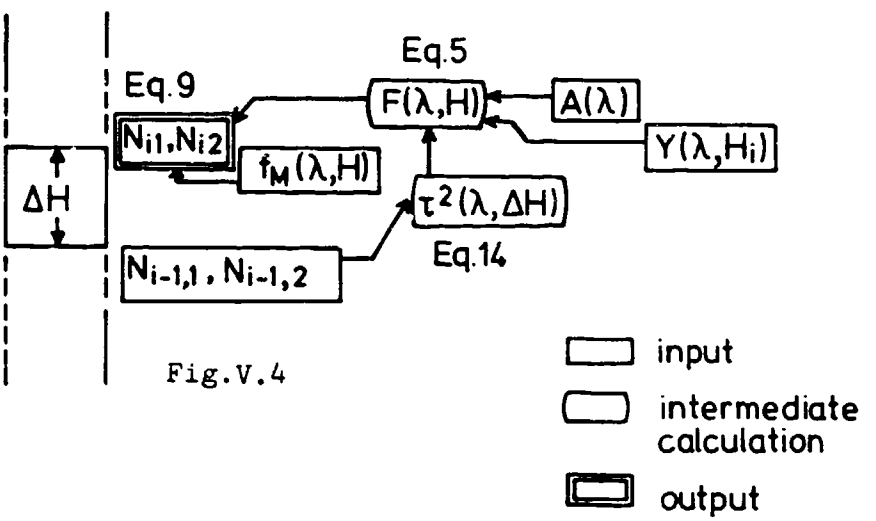

Fig. V. 4

resolution thickness, ΔH, and the lidar signals $Y(\lambda,H)$ for two wavelengths for each height are known, as also $f_m(\lambda,H)$ calculated from Rawinsonde data (7), then if for any height H_i, the two aerosol densities $N_{i-1,1}$, $N_{i-1,2}$

for the bottom of the resolution thickness ΔH, and N_{i1}, N_{i2} for its top be known, $\tau^2(\lambda,\Delta H)$ from equ. (14) and $F(\lambda,H)$ from equ. (9) for both wavelengths can be calculated. With this knowledge and equ. (5) the system constants $A(\lambda)$ for both wavelengths can be calculated (Fig.V.3).

Conversely, if $A(\lambda)$'s and $N_{i-1,1}$, $N_{i-1,2}$ be known then on calculating $\tau^2(\lambda,\Delta H)$ from equation (14) use of equation (5) will give the following two equations for $F_A(\lambda,H)$ in terms of N_{i1} and N_{i2} (Fig.V.4):

$$\Phi^R_{G1}(H_i)\ N_{i1} + \Phi^R_{G2}(H_i)\ N_{i2} = \frac{Y^R}{A^R \cdot \prod_{k=o}^{i} \cdot (\tau^R_k)^2(\Delta H)} - f^R_M(H_i) \quad (15a)$$

$$\Phi^B_{G1}(H_i)\ N_{i1} + \Phi^R_{G2}(H_i)\ N_{i2} = \frac{Y^B}{A^B \cdot \prod_{k=o}^{i} \cdot (\tau^B_k)^2(\Delta H)} - f^B_M(H_i) \quad (15b)$$

N_{i1} and N_{i2} are thus uniquely determined from these linear simultaneous equations.

N_{i1} and N_{i2} can be used, as described in the above paragraph, to calculate $N_{i+1,1}$ and $N_{i+1,2}$. In this way, all N_{i1}'s and N_{i2}'s - the aerosol number densities for fine and coarse aerosols distributed in a bimodal log-normal distribution - can be obtained for (i = 0...n), for a value of n, corresponding to a height from where the lidar signals are still received with a fair accuracy.

Another way of determining the lidar system constants consists in fitting the backscatter signal to a Rayleigh-backscatter signal reduced by a constant extinction due to aerosol scattering.

In a more general form the basic lidar equation (5) reads

$$Y(\lambda,H) = A'(\lambda,H_o)\,\tau_A^2(\lambda,H-H_o)\,\tau_M^2(\lambda,H)\,[f_A(\lambda,H) + f_M(\lambda,H)]$$

with

$$A'(\lambda,H_o) = A(\lambda)\,\tau_A^2(\lambda,H_o) \quad .$$

If the aerosol densities $N_1(H_o)$ and $N_2(H_o)$ are known, the extinction-corrected lidar system constants $A'(\lambda,H_o)$ can be computed from

$$A'(\lambda,H_o) = \frac{Y(\lambda,H_o)}{\tau_M^2(\lambda,H_o)\,[f_A(\lambda,H_o) + f_M(\lambda,H_o)]}$$

and the calculation of the N_i's is performed as above starting from height H_o in downward and upward direction.

In a special case, e.g. above the exchange layer, aerosol scattering may be negligibly small compared to molecular scattering. Then there is a layer with known aerosol densities

$$N_1(H) \simeq N_2(H) \simeq 0 \quad \text{if} \quad H_o \leqq H \leqq H_1 \quad .$$

For our calculations we take ΔH = 1 km and take the first two N-values from the aerological data at Garmisch (740 m a.s.l.) and Wank-peak (1780 m a.s.l.) to obtain the lidar system constants A^R and A^B. To make a check on these values we again calculate them for the next adjacent layer using the Wank and Zugspitze (2963 m a.s.l.) aerological data for the N-values. After finally establishing A^R and A^B as mean of these two calculations the calculation program runs further to calculate the aerosol densities at higher altitudes as described above. A systematic flow diagram is represented in Fig.V.5.

Since N_{i1} and N_{i2} solved from linear equations (15) should be positive, it sets a condition on the absolute values of A^R and A^B. If we solve (15) for N_{i1} and N_{i2} and set the conditions:
$N_{i1} > o$, $N_{i2} > o$, then we obtain

$$\frac{\Phi^R_{G1}}{\Phi^B_{G1}} < \frac{Y^R - f^R_M \cdot A^R \cdot \prod_{k=o}^{i} \cdot \left(\tau^R_k\right)^2}{Y^B \cdot \frac{A^R \cdot \prod_{k=o}^{i} \cdot \left(\tau^R_k\right)^2}{A^B \cdot \prod_{k=o}^{i} \cdot \left(\tau^B_k\right)^2} - f^B_M \cdot A^R \cdot \prod_{k=o}^{i} \cdot \left(\tau^R_k\right)^2} < \frac{\Phi^R_{G2}}{\Phi^B_{G2}}$$

as a typical example, for

$$\Phi_{G1}^{R} = 4.0624 \times 10^{-15}\ m^2 \times sterad^{-1}$$

$$\Phi_{G2}^{R} = 5.3653 \times 10^{-13}\ m^2 \times sterad^{-1}$$

$$\Phi_{G1}^{B} = 1.9469 \times 10^{-14}\ m^2 \times sterad^{-1}$$

$$\Phi_{G2}^{B} = 3.0871 \times 10^{-13}\ m^2 \times sterad^{-1}$$

$$f_{M}^{R} = 4 \times 10^{-7}\ m^{-1} \times sterad^{-1}$$

$$f_{M}^{B} = 6 \times 10^{-6}\ m^{-1} \times sterad^{-1}$$

$$A^{R} = 4 \times 10^{7}$$

$$A^{B} = 4 \times 10^{5}$$

$$\prod_{k=o}^{i} (\tau_k^R)^2 = 0.75$$

$$\prod_{k=o}^{i} (\tau_k^B)^2 = 0.5$$

The inequality (16) becomes

$$0.2 < \frac{Y^R - 12}{150\,Y^B - 180} < 1.7$$

Plotted on a graph in Fig.V.6, the shaded region gives the permissible values of Y^R and Y^B.

VI. CALCULATION OF RAYLEIGH- AND MIE-SCATTERING COEFFICIENTS

1. Molecular Scattering

Radiosonde soundings yield pressure p_j, temperature T_j and relative humidity RH_j for each baroswitch click j. From this basic set of data the corresponding altitudes H_j and water vapor pressures e_j are calculated.

According to the Rayleigh scattering theory (GOODY 1964), the molecular volume scattering coefficient is given by

$$\sigma_{M,j}(\lambda) = \frac{32\pi^3}{3} \cdot \lambda^{-4} \cdot \frac{(m_j(\lambda)-1)^2}{N_j} \cdot \frac{3(2+\Delta)}{6-7\Delta}$$

with molecular density $N_j = 0.72435 \cdot 10^{25} \frac{p_j[mb]}{T_j[K]}\ m^{-3}$

The index of refraction is related to pressure, temperature and water vapor pressure by

$$(m_j(\lambda)-1) \cdot 10^6 = A(\lambda)\ \frac{p_j}{T_j} - \delta(m_j(\lambda)-1)$$

with A (0.6943μ) = 78.39,
A (0.3472μ) = 81.38,

(p_j is measured in mb and T_j in K)

and the water vapor pressure correction

$$\delta\,(m_j(\lambda)-1)\cdot 10^{-6} = \begin{cases} 12.5\,\dfrac{e_j[\mathrm{mb}]}{T_j[\mathrm{K}]}, & \lambda = 0.6943\mu\ , \\ 11.6\,\dfrac{e_j[\mathrm{mb}]}{T_j[\mathrm{K}]}, & \lambda = 0.3472\mu\ . \end{cases}$$

The mean depolarization factor for air is $\Delta = 0.035$.

Thus we obtain the molecular volume scattering coefficients

$$\sigma_{M,j}(0.6943\mu)\mathrm{m}^{-1} = 1.28\cdot 10^{-6}(1-0.16\,\frac{e}{p})^2\,\frac{p[\mathrm{mb}]}{T[\mathrm{K}]},$$

$$\sigma_{M,j}(0.3472\mu)\mathrm{m}^{-1} = 2.21\cdot 10^{-5}(1-0.14\,\frac{e}{p})^2\,\frac{p[\mathrm{mb}]}{T[\mathrm{K}]}.$$

The transmissivity $\tau_j(\lambda)$ is computed from the scattering coefficients by

$$\tau_j(\lambda) = \exp\left(-\sum_{i=0}^{j}\sigma_{i,m}(\lambda)\,\Delta H_i\right)\ ,\ \Delta H_i = H_i - H_{i-1},\ \Delta H_o = 0.$$

Two tables are built up, one containing altitude, temperature, relative humidity, Rayleigh scattering coefficients and transmissivities for each baroswitch click (table RAY1) (Tab.VI.1), another one containing H_i, RH_i, $\sigma^R_{M,i}$ and $\sigma^B_{M,i}$ ($i = 0\ldots i_{max}$), interpolated for a series of fixed levels H_i, e.g. from 1000 m a.s.l. to 3000 m a.s.l.

Tab.VI.1

Rayleigh scattering coefficients and transmissivities

26.02.75/09.36

H	T	RF	SIGMA-ROT	TAU-ROT	SIGMA-BLAU	TAU-BLAU
00735	-04.2	085.0	.45136E-05	.*****	.77668E-04	.*****
00789	-05.[illegible]	072.0	.44866E-05	.99976	.77370E-04	.99581
00882	-04.7	076.3	.44286E-05	.99935	.76371E-04	.98880
00971	-05.0	077.4	.43835E-05	.99896	.75594E-04	.98215
01061	-05.0	075.9	.43334E-05	.99857	.74730E-04	.97554
01153	-05.1	072.4	.42859E-05	.99817	.73911E-04	.96897
01263	-05.[illegible]	068.0	.42240E-05	.99771	.72842E-04	.96123
01352	-04.7	064.6	.41716E-05	.99734	.71938E-04	.95507
01452	-05.0	062.8	.41239E-05	.99693	.71117E-04	.94834
01543	-05.1	059.0	.40788E-05	.99656	.70337E-04	.94227
01636	-05.1	053.6	.40313E-05	.99619	.69518E-04	.93623
01753	-05.[illegible]	047.3	.39696E-05	.99572	.68454E-04	.92875
01843	-03.6	041.6	.39043E-05	.99537	.67326E-04	.92311
01940	-03.6	038.2	.38569E-05	.99500	.66510E-04	.91720
02033	-04.4	038.1	.38228E-05	.99465	.65922E-04	.91161
02131	-05.1	037.5	.37861E-05	.99428	.65287E-04	.90576
02251	-05.9	036.8	.37394E-05	.99383	.64482E-04	.89881
02346	-06.8	035.8	.37065E-05	.99348	.63915E-04	.89333
02443	-07.5	035.6	.36711E-05	.99313	.63305E-04	.88788
02535	-08.4	035.9	.36399E-05	.99279	.62766E-04	.88275
02634	-09.0	038.0	.36019E-05	.99244	.62110E-04	.87738
02733	-09.9	040.5	.35689E-05	.99209	.61542E-04	.87203
02828	-10.4	045.6	.35314E-05	.99176	.60894E-04	.86700
02929	-10.9	045.7	.34908E-05	.99141	.60195E-04	.86172
03026	-11.8	044.3	.34595E-05	.99107	.59655E-04	.85674
03125	-11.9	043.0	.34161E-05	.99074	.58906E-04	.85180
03246	-10.9	041.3	.33493E-05	.99034	.57754E-04	.84583
03342	-10.7	041.0	.33059E-05	.99002	.57007E-04	.84122
03439	-10.9	041.7	.32662E-05	.98971	.56322E-04	.83664
03543	-11.6	042.7	.32311E-05	.98938	.55716E-04	.83181
03636	-12.1	043.1	.31989E-05	.98908	.55161E-04	.82754
03766	-12.3	043.8	.31466E-05	.98868	.54259E-04	.82173
03868	-12.8	043.6	.31116E-05	.98837	.53656E-04	.81725
03971	-13.5	044.2	.30781E-05	.98805	.53079E-04	.81280
04075	-14.0	045.2	.30411E-05	.98774	.52440E-04	.80837
04174	-14.5	045.0	.30081E-05	.98744	.51871E-04	.80422
04281	-15.4	044.7	.29756E-05	.98713	.51311E-04	.79984
04382	-15.6	045.1	.29390E-05	.98684	.50680E-04	.79574
04485	-16.6	046.9	.29102E-05	.98654	.50182E-04	.79165
04589	-17.0	046.5	.28748E-05	.98625	.49573E-04	.78760
04700	-17.3	046.0	.28354E-05	.98594	.48892E-04	.78331
04827	-17.7	045.3	.27923E-05	.98559	.48150E-04	.77855
04935	-18.6	045.0	.27625E-05	.98529	.47636E-04	.77456
05037	-19.2	042.9	.27307E-05	.98502	.47086E-04	.77083
05148	-20.2	040.4	.27019E-05	.98473	.46590E-04	.76688
05245	-20.5	039.6	.26693E-05	.98447	.46028E-04	.76344
05380	-21.8	038.8	.26349E-05	.98412	.45434E-04	.75879
05487	-22.3	037.2	.26011E-05	.98385	.44851E-04	.75515

in steps of 50 m (table RAY2) (see the first four columns of Tab.VII.1). Table RAY2 is stored on magnetic tape or disk.

2. Aerosol Scattering

Originally the aerosol extinction efficiencies K_E (c.f. V.4) were calculated after PENNDORF and DEIRMENDJIAN formulae given in HÄNEL (1970). The computation of the aerosol backscattering function f_A requires the evaluation of the MIE-function for backscattering

$$i(\alpha,m,180^\circ) = \left| \sum_{n=1}^{\infty} (n+1/2) \cdot (-1)^{n+1} \cdot (a_n - b_n) \right|^2,$$

where α is the size parameter, m the complex index of refraction and a_n and b_n are the complex MIE-scattering coefficients given by

$$a_n(\alpha,m) = \frac{\left(\frac{A_n}{m} + \frac{n}{\alpha}\right) \cdot \mathrm{Re}\,\xi_n - \mathrm{Re}\,\xi_{n-1}}{\left(\frac{A_n}{m} + \frac{n}{\alpha}\right) \cdot \xi_n - \xi_{n-1}}$$

$$b_n(\alpha,m) = \frac{\left(mA_n + \frac{n}{\alpha}\right) \cdot \mathrm{Re}\,\xi_n - \mathrm{Re}\,\xi_{n-1}}{\left(mA_n + \frac{n}{\alpha}\right) \cdot \xi_n - \xi_{n-1}}$$

The function $A_n(m\alpha)$ can be computed using the recurrence relation

$$A_n(m\alpha) = -\frac{n}{m\alpha} + \frac{1}{\frac{n}{m\alpha} - A_{n-1}(m\alpha)}$$

and $A_o(m\alpha) = \cot(m\alpha)$.

The function $\xi_n(\alpha)$ is also given by recurrence:

$$\xi_n(\alpha) = \frac{2n-1}{\alpha}\ \xi_{n-1}(\alpha) - \xi_{n-2}(\alpha)\ ,$$

and $$\xi_{-1}(\alpha) = \cos\alpha - i \cdot \sin\alpha\ ,$$

$$\xi_o(\alpha) = \sin\alpha + i \cdot \cos\alpha\ .$$

As the extinction efficiency can also be expressed in terms of the functions a_n and b_n by

$$K_E(\alpha,m) = \frac{1}{\alpha^2} \sum_{n=1}^{\infty} (2n+1)\ (\mathrm{Re}\ a_n + \mathrm{Re}\ b_n)\ ,$$

extinction efficiency and backscattering MIE-function will be evaluated and tabulated in the same run for a given set of size parameters and index of refraction. Numerical integration of these tabulated values over the assumed log-normal particle size distribution then yields the required collective values K_G and i_G for given refractive index m and a log-normal size distribution characterized by its mean size parameter α_m and standard deviation s (Tab.VI.2).

Tab.VI.2

Backscattering MIE-functions for log-normal size distributions*

RH, %	Refr. Index	$i_G(\alpha_1^R)$	$i_G(\alpha_2^R)$	$i_G(\alpha_1^B)$	$i_G(\alpha_2^B)$
0	1.62 -i 0.02	0.3327	43.94	6.378	101.1
50	1.605-i 0.018	0.3207	44.0	6.195	98.89
70	1.57 -i 0.0164	0.2916	40.42	5.609	91.87
80	1.47 -i 0.0097	0.2173	20.44	4.085	68.33
85	1.42 -i 0.0075	0.1763	16.51	3.31	.....

* The mean size parameters are α_1^R=1.71, α_2^R=9.04, α_1^B=3.42, α_2^B=18.08, the standard deviation is 0.3.

VII. THE EVALUATION ROUTINE - COMPUTATIONAL FLOW AND APPLICATION TO ABSOLUTE LIDAR CALIBRATION, AEROSOL DENSITY AND SIZE DISTRIBUTION PROFILES

1. Data Processing

Data processing occurs in two steps. In the first step the digital backscatter data edited on paper tape by the fast transient recorder have to be normalized and corrected for the square of height, smoothed and plotted for control and qualitative evaluation. The backscatter data are stored on magnetic tape or disk in two tables, one for each lidar frequency.

In a second step lidar data and Rayleigh scattering data are combined into one table, calibrated and evaluated according to the iteration method described in section V.5 in order to obtain the aerosol profiles.

a) Normalization of the backscatter data

The output of the transient recorder consists of digital backscatter signals $\bar{Y}'_j(\lambda)$ for 2000 sample intervals j per frequency λ, divided into two ranges of different amplification and two ranges of different time base.

The second time base - for the last 200 sample intervals - is comparatively long (500ns = 75m) and it is assumed that the mean signal contained in the last 50 sample intervals represents the skylight background and determines the zeroline of the second amplification range. The condition of steadiness at the switching point between the two amplification ranges together with the known amplification ratio enables the computation of the zeroline in the first amplification range.

The height-corrected, normalized backscatter signal is given by

$$Y_j = Q \cdot \bar{Y}'_j \cdot (H_j^2 + b)/E ,$$

where $\bar{Y}'_j$: background-corrected signal,
H_j: mean altitude corresponding to sample interval j,
E : emitted laser energy,
Q : normalization constant containing photomultiplier h.v., amplification factor, transient recorder input sensitivity,
b : defocussing correction for signals received from lower altitudes.

In order to obtain a reasonable normalized backscatter signal and calibrated aerosol profiles, several parameters may have to be varied during the calculations and the effect of these variations at the different stages of the data processing should be visualized immediately. To this purpose a flexible operation system was developed for our minicomputer, using the graphical display terminal, fast incremental plotter and fast line-printer. The following flowcharts (Fig.VII.1) indicate the regular flow of calculations. Each operation in this sequence may be restarted with changed parameters and is controlled through instant graphical output.

b) Iterative computation of aerosol density and size distribution (cf.V.5).

The main iteration program is operating on the complete table containing altitude H_i, relative humidity RH_i, molecular scattering coefficients $\sigma^R_{M,i}$ for red and $\sigma^B_{M,i}$

for UV lidar frequencies and height-corrected lidar backscatter signals Y_i^R and Y_i^B for $i = 0...i_{max}$. Parameters of the calculations are:

- the mean size parameters $\alpha_{m,1}$ and $\alpha_{m,2}$ and the standard deviations s_1 and s_2 of the two log-normal distributions characterizing the aerosol size distribution,

- the calibration constants A^R and A^B (or more general $A^{R'}$ and $A^{B'}$ (cf.V.5)).

For our first calculations we choose size parameters $\alpha = \pi D/\lambda$ corresponding to particle diameters $D_1 = 0.38\mu$ and $D_2 = 2\mu$ and standard deviations $s_1 = s_2 = 0.3$, which fit well to the size distributions measured at our three stations (see also BARTUSEK et.al. (1970)).

As the index of refraction and therefore the extinction efficiency dG (cf.V.4) and scattering function Φ (cf.V.3) depend on relative humidity, a table of dG's and Φ's as functions of relative humidity has to be provided for the calculations. For the moment we only use values of dG and Φ calculated for one complex index of refraction m = 1.62 - 0.02i, supposed to be valid for a relative humidity range between 0 - 50% .

Finally the starting values $N_{1,o} = N_1(H_o)$ and $N_{2,o} = N_2(H_o)$ have to be fixed either by measurement at one of our mountain stations or by the assumption of a pure Rayleigh scattering case at $H = H_o$.

The flowchart of the main program is given below (Fig.VII. 2). The program calls several subroutines. One of them is intended to look up the values for $dG(RH_i, \alpha_1^R, s_1)$, $dG(RH_i, \alpha_2^R, s_2)$, $dG(RH_i, \alpha_1^B, s_1)$ and $dG(RH_i, \alpha_2^B, s_2)$ and $\Phi(RH_i, \alpha_1^R, s_1)$, $\Phi(RH_i, \alpha_2^R, s_2)$, $\Phi(RH_i, \alpha_1^B, s_1)$ and

$\Phi(RH_i, \alpha_2^B, s_2)$ in a precomputed table for a given set of humidity intervals. The other subroutines are function subroutines to evaluate the aerosol backscattering functions $f_{A,i}$ as functions of Y_i, $\sigma_{M,i}$, ΔH_i, $N_{1,i-1}$ and $N_{2,i-1}$ using the formulae

$$f_{A,i} = \frac{Y_i}{A\tau_{A,i}^2\ \tau_{M,i}^2} - f_{M,i} ,$$

where $f_{M,i} = \frac{3}{8\pi}\ \sigma_{M,i}$, $\tau_i^2 = \tau_{i-1}^2 \exp(-2\sigma_i \Delta H_i)$

and $\sigma_{A,i} = N_{1,i-1}\ dG_1 + N_{2,i-1}\ dG_2$.

The output of the iteration program includes computer plots of the two density profiles $N_1(H)$ and $N_2(H)$ for fine and coarse aerosol (Fig.VII.4) and a tabulation of the complete data set (Tab.VII.1), which is the basis of the iteration calculations.

2. A First Example for the Application of the Evaluation Routine

The example is taken from a series of lidar firings made on February 26, 1975 at 0940 CET. It coincides with

- a radiosonde ascent (Tab.VII.1, first part),
- data transmission from the Zugspitze cable-car telemetry system (Fig.VII.4),
- simultaneous measurements of the aerosol size distribution at the three stations (Fig.VII.3a,b,c).

Tab.VII.1

Particle density profiles from lidar backscatter signals

26.02.75/09.40

H, m	RH, %	σ_m^R, m^{-1}	σ_m^B, m^{-1}	Y^R	Y^B	N_1,part/m^3	N_2,part/m^3
00755	06 .2	.44974E-05	.77558E-04	17.13	24.85	0.10E+09	0.16E+06
010 0	076.9	.43675E-05	.75318E-04	35.99	45.93	0.37E+09	0.76E+06
01050	076.1	.43398E-05	.74840E-04	34.81	44.11	0.38E+09	0.61E+06
011 0	074.4	.43134E-05	.74384E-04	33.68	41.51	0.35E+09	0.75E+06
01150	072.5	.42874E-05	.73936E-04	33.98	38.77	0.32E+09	0.70E+06
012 0	07 .5	.42594E-05	.73453E-04	28.69	38.44	0.34E+09	0.27E+06
01250	068.5	.42313E-05	.72968E-04	28.52	36.59	0.32E+09	0.52E+06
013 0	066.6	.42023E-05	.72467E-04	26.46	32.83	0.26E+09	0.74E+06
01350	064.7	.41729E-05	.71962E-04	26.27	32.40	0.27E+09	0.68E+06
014 0	063.7	.41487E-05	.71544E-04	25.87	29.65	0.22E+09	0.11E+07
01450	062.8	.41248E-05	.71131E-04	24.71	27.59	0.18E+09	0.12E+07
015 0	06 .8	.410 1E-05	.707 5E-04	24.08	26.63	0.17E+09	0.12E+07
01550	058.6	.40753E-05	.70276E-04	22.53	25.05	0.15E+09	0.12E+07
016 0	055.7	.40496E-05	.69833E-04	17.02	23.23	0.12E+09	0.63E+06
01650	052.8	.40237E-05	.69387E-04	13.52	21.16	0.86E+08	0.41E+06
017 0	05 .2	.39974E-05	.68933E-04	12.34	19.60	0.55E+08	0.48E+06
01750	047.5	.39711E-05	.68479E-04	11.28	19.18	0.57E+08	0.19E+06
018 0	044.3	.39355E-05	.67865E-04	09.48	18.71	0.55E+08	0.86E+05
01850	041.4	.39010E-05	.67269E-04	09.26	18.34	0.54E+08	0.79E+05
019 0	039.6	.38765E-05	.66847E-04	09.03	17.97	0.25E+08	0.27E+06
01950	038.2	.38532E-05	.66446E-04	08.88	16.69	0.21E+08	0.29E+06
020 0	038.1	.38348E-05	.66128E-04	08.79	16.47	0.21E+08	0.27E+06
02050	038.0	.38164E-05	.65810E-04	08.23	17.45	0.58E+08	0.00E+00
021 0	037.7	.37977E-05	.65488E-04	08.03	15.89	0.18E+08	0.21E+06
02150	037.4	.37787E-05	.65160E-04	08.07	13.32	0.00E+00	0.41E+06
022 0	037.1	.37592E-05	.64824E-04	07.65	13.08	0.00E+00	0.34E+06
02250	036.8	.37397E-05	.64487E-04	07.16	12.95	0.00E+00	0.27E+06
023 0	036.3	.37225E-05	.64190E-04	06.80	11.18	0.00E+00	0.21E+06
02350	035.8	.37052E-05	.63892E-04	06.73	13.22	0.00E+00	0.20E+06
024 0	035.7	.36869E-05	.63576E-04	06.69	9.78	0.00E+00	0.19E+06
02450	035.6	.36688E-05	.63263E-04	06.37	09.89	0.00E+00	0.15E+06
025 0	035.8	.36519E-05	.62972E-04	06.22	08.30	0.00E+00	0.13E+06
02550	036.2	.36342E-05	.62668E-04	06.24	08.41	0.00E+00	0.14E+06
026 0	037.3	.36149E-05	.62334E-04	06.14	08.14	0.00E+00	0.12E+06
02650	038.4	.35965E-05	.62016E-04	06.14	05.83	0.00E+00	0.13E+06
027 0	039.7	.35799E-05	.61730E-04	06.24	04.71	0.00E+00	0.15E+06
02750	041.4	.35622E-05	.61425E-04	05.67	03.97	0.00E+00	0.61E+05
028 0	044.1	.35424E-05	.61085E-04	05.54	05.11	0.00E+00	0.46E+05
02850	045.6	.35226E-05	.60742E-04	05.59	03.91	0.00E+00	0.56E+05
029 0	045.6	.35026E-05	.60397E-04	05.15	04.13	0.00E+00	0.00E+00
02950	045.4	.34842E-05	.60080E-04	04.94	02.44	0.00E+00	0.00E+00
030 0	044.7	.34681E-05	.59812E-04	05.06	02.86	0.00E+00	0.00E+00

Although lidar data were recorded up to a maximum height of 6750 m a.s.l. and radiosonde data are available up to 29 km, the evaluation was limited to a maximum height of 3000 m a.s.l.. This is the range where detailed comparison with aerological and aerosol measurements is possible.

This comparison is shown in Fig.VII.4. The aerosol density profiles fit fairly well to the particle concentrations derived from the impactor measurements carried out at Wank peak (denoted by W_1 and W_2) and at Zugspitze (denoted by Z_1 and Z_2). This is the result of the calibration routine, the aim of which is to find a consistent set of parameters for both lidar frequencies, viz. the lidar system constants A^R and A^B, the zerolines for both amplification ranges and the defocussing correction constants. Fitting the computed aerosol density profiles to the measured values is not yet carried out completely automatically, because the change of a parameter for one lidar frequency affects both aerosol density profiles (the backscatter intensity of light of any frequency is due to coarse and fine aerosol) and may have to be compensated partly by a change of a parameter for the other frequency etc. in order to reach consistency. The effect of this interdependence of both profiles $N_1(H)$ and $N_2(H)$ can be seen in Fig.VII.4. An increase in the fine aerosol concentration is accompanied rather frequently by a decrease in the coarse aerosol concentration or vice versa. Certainly this is not always true in reality and may be the result of a fluctuation in one of the backscatter signals.

On the other hand a simultaneous decrease in both fine and coarse aerosol densities indicates a real effect as can be seen from a comparison between the atmospheric conductivity profiles and the aerosol profiles in Fig. VII.4. In this example the conductivity profiles together

with the temperature profile suggest the presence of roughly four layers between 1000 m and 3000 m a.s.l.. The haze layer (1000 - 1500 m) is characterized by a high concentration of both fine and coarse aerosol. Above the haze layer there is a layer with increasing atmospheric conductivity. This means a decrease of particle number concentration. Actually the aerosol concentration profiles obtained from lidar backscatter data show this behavior. Above the inversion at 1900 m the conductivity decreases again. Possibly the increase if coarse aerosol concentration at this altitude together with the fine aerosol density remaining constant may be interpreted as a precondensation effect within this layer. In the fourth layer (2200 - 2800 m) the coarse aerosol concentration decreases to a value of the same order as the one measured at Zugspitze peak. The absence of fine aerosol data simply means that in the course of the evaluation routine negative particle concentrations occurred probably due to an overestimation of the 347 nm backscatter signal background. At this stage the iteration computations should be restarted with changed parameters. As mentioned above, the then resulting increase in the fine aerosol concentration would necessarily be accompanied by a decrease in the coarse aerosol density.

Definition of Symbols

Note: The superscript R or B above a symbol indicates that it corresponds to the wavelength 0.6943μ or 0.3472μ, respectively.

Symbol	Definition
A	Constant for lidar system
d_E	Extinction coefficient of a single particle, $= \pi r^2 K_E$
d_G	Extinction coefficient of log-normal-distributed particle collective, normalized for a single particle, $= (\lambda^2 \alpha_m^2 / 4\pi) K_G$
D	Diameter
D_m	Median diameter of a log-normal distribution
f_A	Volume scattering function for aerosol
f_M	Volume scattering function for atmospheric molecules
g	Relative humidity
H	Height above lidar station
K_E	Extinction cross-section of a particle
K_G	Extinction cross-section of a log-normal distribution of particle collective, normalized for a single particle; equation (12b)
i	Mie-function for backscattering
i_G	Mie-function of a log-normal distribution of particle collective, normalized for a single particle, equation (8b)
m_A	Complex refractive index of aerosol and air, respectively

Definition of Symbols (cont)

$n(D)$	Aerosol size distribution function
N_M	Molecular number density
N_1, N_2	Aerosol number densities for the fine and coarse aerosols, respectively, of a bimodal log-normal distribution
P	Pressure
Q	Lidar pulse energy
r	Aerosol radius
R	Load resistance of the photomultiplier
S	Spectral sensitivity of the photomultiplier
s	Logarithmic standard deviation of log-normal particle size distribution
T	System optical efficiency
W	Lidar power signal
α	Scattering parameter = $\frac{\pi D}{\lambda}$
λ	Wavelength
σ_M, σ_A	Molecular and aerosol extinction coefficients respectively
$\tau(\Delta H)$	Transmissivity of atmospheric layer thickness ΔH, equation (10)
Φ_G	Volume backscattering function for a log-normal distribution of particles, normalized for a single particle, equations (8a) and (8b)
Σ	Effective area of the receiver

VIII. CONCLUSIONS

1. Lidar System

The technical development of the lidar system may now be considered as to be essentially finished. In its present layout the system meets all requirements to be made. The reliability of its operation, however, should be further improved by providing more spare parts, especially optical components (ruby, mirrors, glass plates, frequency doubler etc.) and some electronic components.
Future developments in electronics (e.g. A-D converters with increased resolution) and optics (more efficient and notwithstanding durable frequency doubling materials) should be considered and utilized.

2. Data Processing

Our computer system, after all programs being essentially completed, is now fully capable of performing all data evaluation work as well as all the extensive calculations described in sections V to VII of this report. Nevertheless, additional on-line, real-time data processing would be desirable, especially in connection with photon counting. In this case, it is more difficult to get a first survey of the results immediately after the measurement.

3. Theoretical Procedures

The fundamentals of the theoretical evaluation and calibration procedures may be considered as completed. With the experiences gained at the evaluation of the systematic calibration measurements to be performed in the near future, some changes and improvements could turn out to

be necessary. The main difficulty in the procedure is the somewhat unsatisfactory resolution of the 347 nm signals, even if, due to minor defects of some optical parts, the transmitter output power in that wavelength was reduced at the time the first calibration measurements were performed. With the present development of new, more efficient types of frequency doublers, improvements in this field are to be expected in the future.

4. Calibration of the Lidar System

The first results available of absolute calibration measurements using aerosol data from the mountain stations indicate the procedure to be applicable in principle. It has to be improved, however, in some details, after much more empirical data for calibration have been collected.

IX. FUTURE PLANS

a) As the lidar system is now essentially completed, only a few technical improvements are to be carried out in the future:
on-line data processing, new A-D converters, using more efficient frequency doublers.

b) The reliability of the system is to be further improved, among other things by providing additional spare parts.

c) systematic calibration measurements are to be carried out, together with simultaneously obtaining of aerosol and aerological data by the mountain stations, by the cable-car equipment and by means of the radiosondes.

d) With the calibration of the system completed, it is to be used for practical work in remote sensing of aerosols, including systematic night-time high al-

titude measurements with photon counting. In these cases, simultaneous night-time radiosonde ascents are possible and necessary, since the routine weather service data are insufficient for this purpose.

e) The theoretical procedures worked out in the past are to be applied for evaluation of data, and to be improved if necessary. The tables of Mie-functions should be extented by calculating the functions for more values of the complex index of refraction. The influence of humidity is to be considered. Finally, high altitude measurements with photon counting must be included.

f) A second, mobile lidar system is under construction and will be available in the beginning of 1976. This system, besides a ruby laser with frequency doubler, will be equipped with an additional frequency doubled Neodymium glass laser allowing firings in 553 nm wavelength. With this mobile three frequency lidar, especially in connection with the first system, vertical and horizontal variations of aerosol constitution as well as processes of cloud formation and disintegration are to be studied. The third wavelength will involve considerable modifications of the mathematical procedures.

X. REFERENCES

BARTUSEK, K., D.J. GAMBLING and W.G. ELFORD: Stratospheric aerosol measurements by optical radar. J. Atmos. Phys. 32, 1535 (1970).

COLLIS, R.T.H.: Lidar. Applied Optics, Vol. 9, 1782 (1970).

FOITZIK, L., G. SCHEITHAUER and D. SPÄNKUCH: Z. f. Met., 21, 99 (1969).

GOODY, R.M.: Atmospheric radiation. I:Theoretical Basis, P. 389, Clarendon Press, Oxford (1964).

HÄNEL, G.: The real part of the mean complex refractive index and the mean density of samples of atmospheric aerosol particles. Tellus, XX, 3 (1968).

HÄNEL, G.: The size of atmospheric aerosol particles as a function of the relative humidity. Beiträge zur Physik d. Atmosphäre, 43, 119 (1970).

HÄNEL, G.: New results concerning the dependence of visibility on relative humidity and their significance in a model for visibility forecast. Beiträge zur Physik d. Atmosphäre, 44, 137 (1971).

HÄNEL, G.: Computation of the extinction of visible radiation by atmospheric aerosol particles as a function of the relative humidity, based upon measured properties. J. Aerosol Science, Vol. 3, 377 (1972).

JUNGE, C. and R. JAENICKE: New results in background aerosols studies from the Atlantic Expedition of the R.V. Meteor, Spring 1969. J. Aerosol Science, Vol. 2, No. 3, 305 (1971).

KATÉRLE, H.-J.: Die Messung der Rückwärtsstrahlung an Molekülen und Aerosolen in der Stratosphäre mittels Rubin-Laserstrahlen vom Boden aus. Thesis University of München (1970).

McCORMICK, M.P.: Simultaneous multiple wavelength laser radar measurements of the lower atmosphere. Presented at the Electro-Optics International Conference, Brighton, England, March 24-26, 1971 (1971).

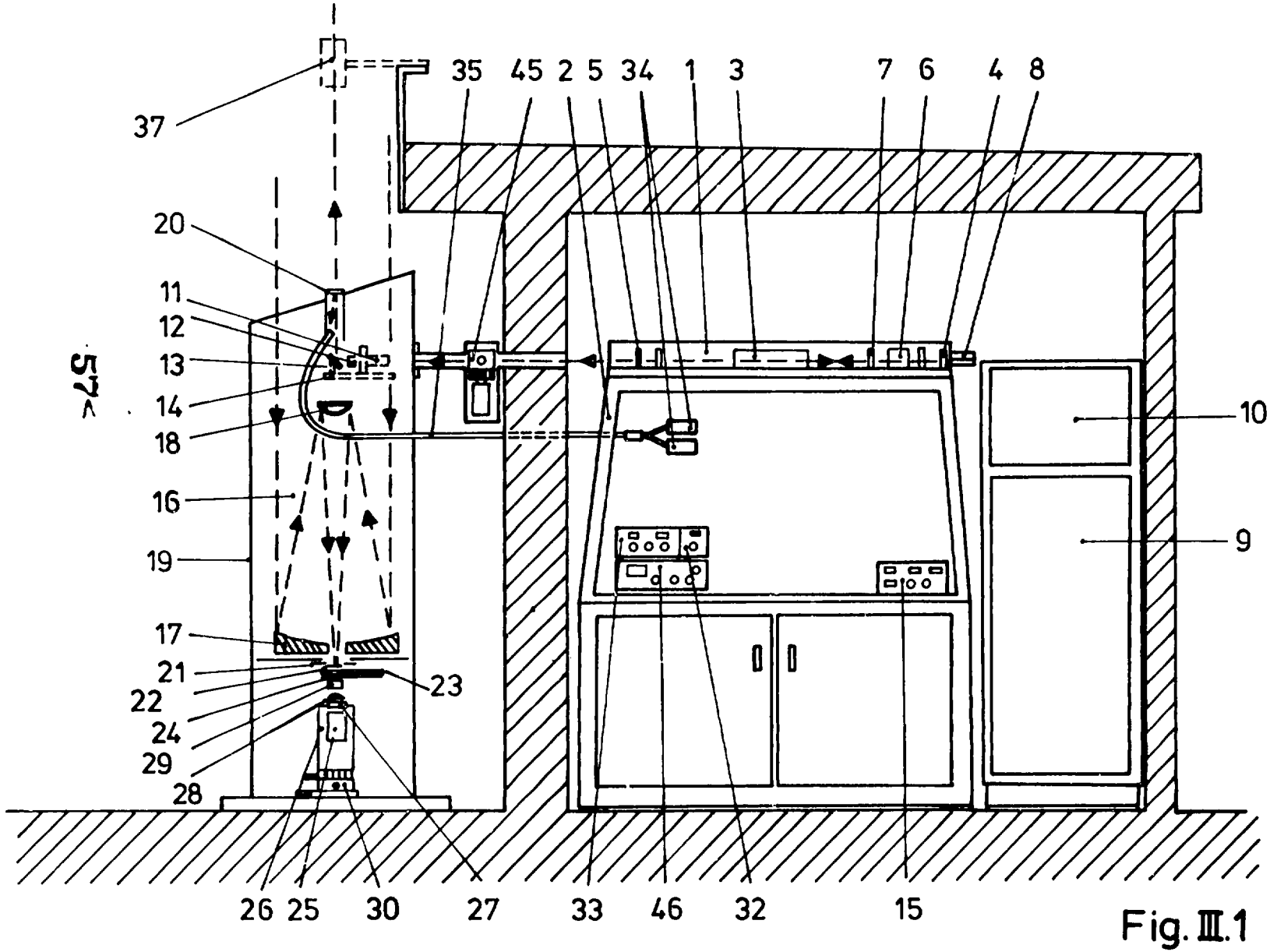
37
35
45
2
5
34
1
3
7
6
4
8
20
11
12
13
14
18
16
19
17
21
22
24
29
28
23
10
9
26
25
30
27
33
46
32
15

Fig. III.1

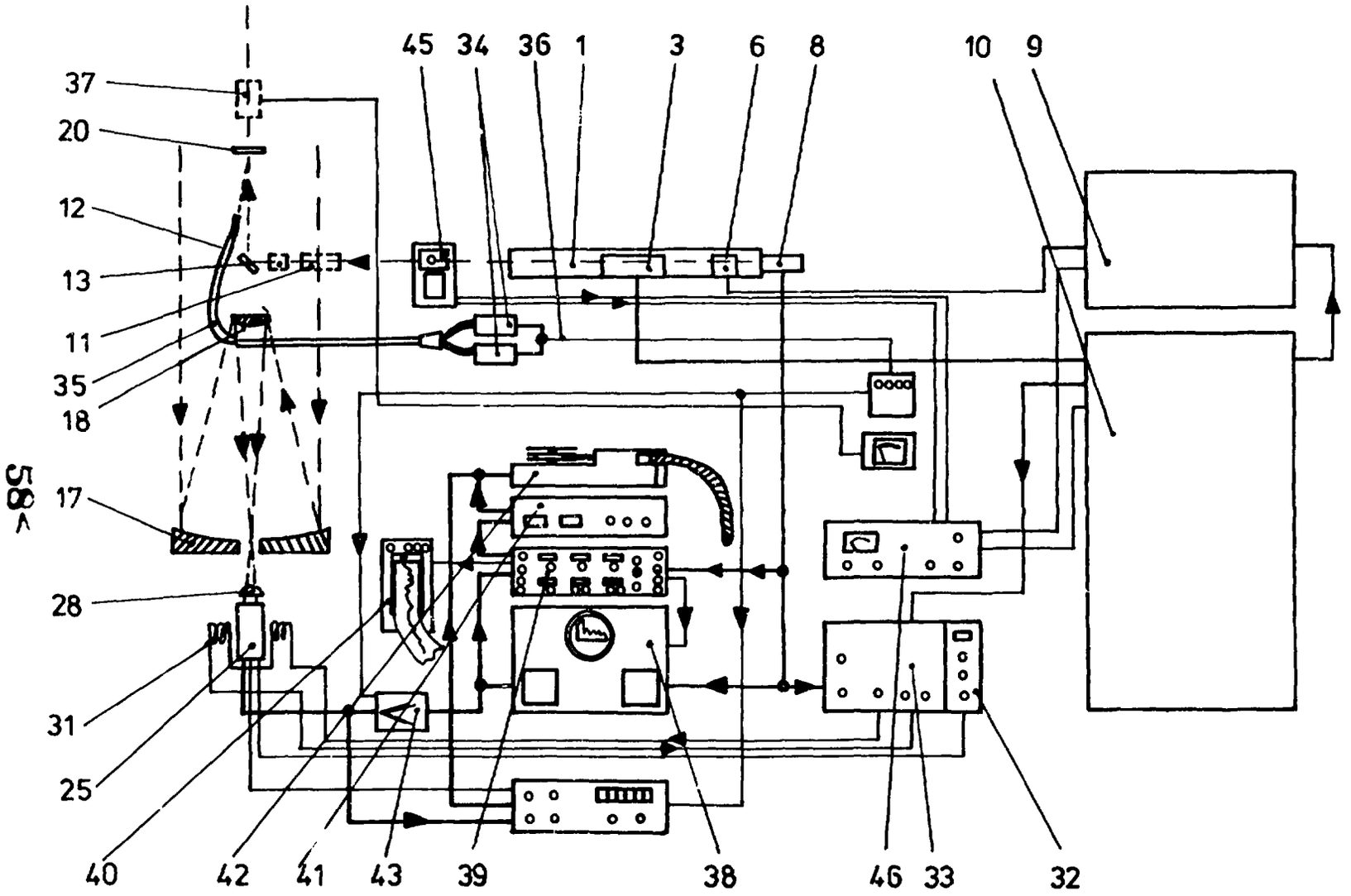
45
34
36
1
3
6
8
10
9
37
20
12
13
11
35
18
17
28
31
25
40
42
41
43
39
38
46
33
32

Fig. III.2

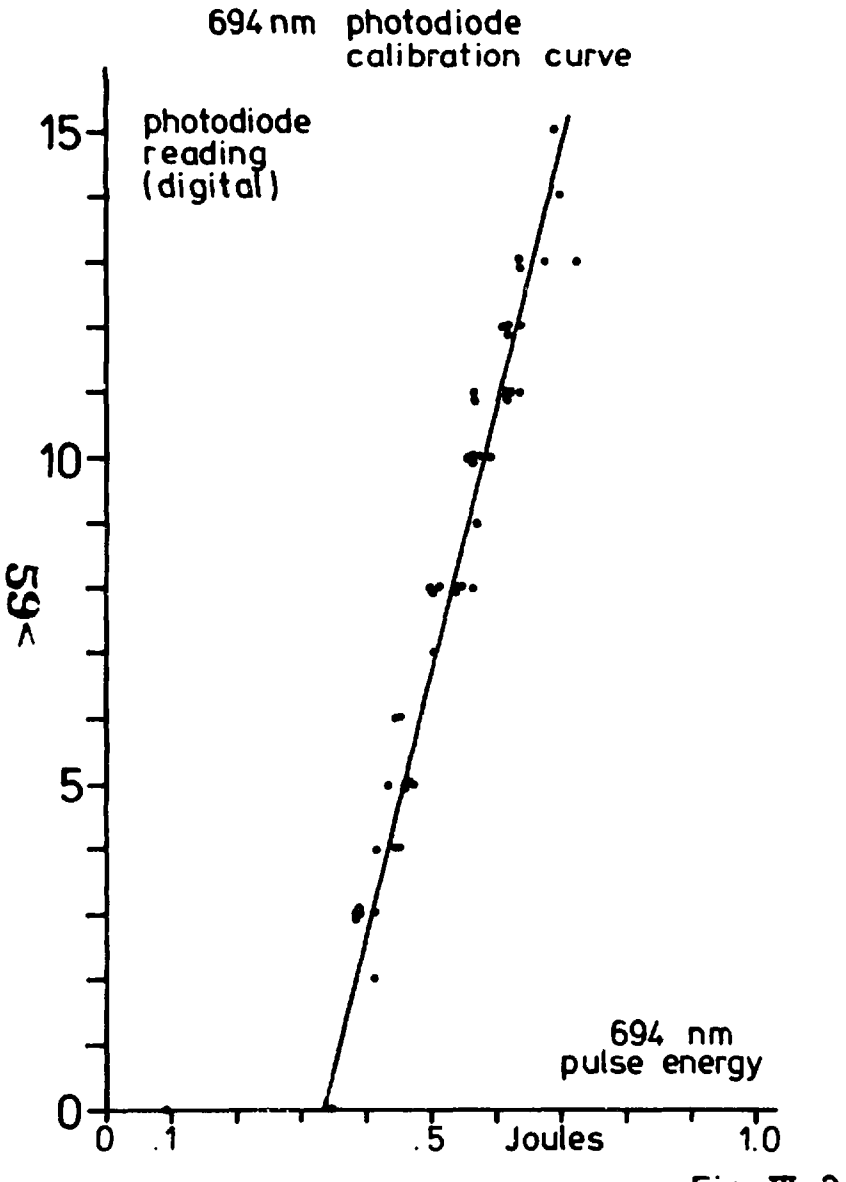

Fig. III. 3

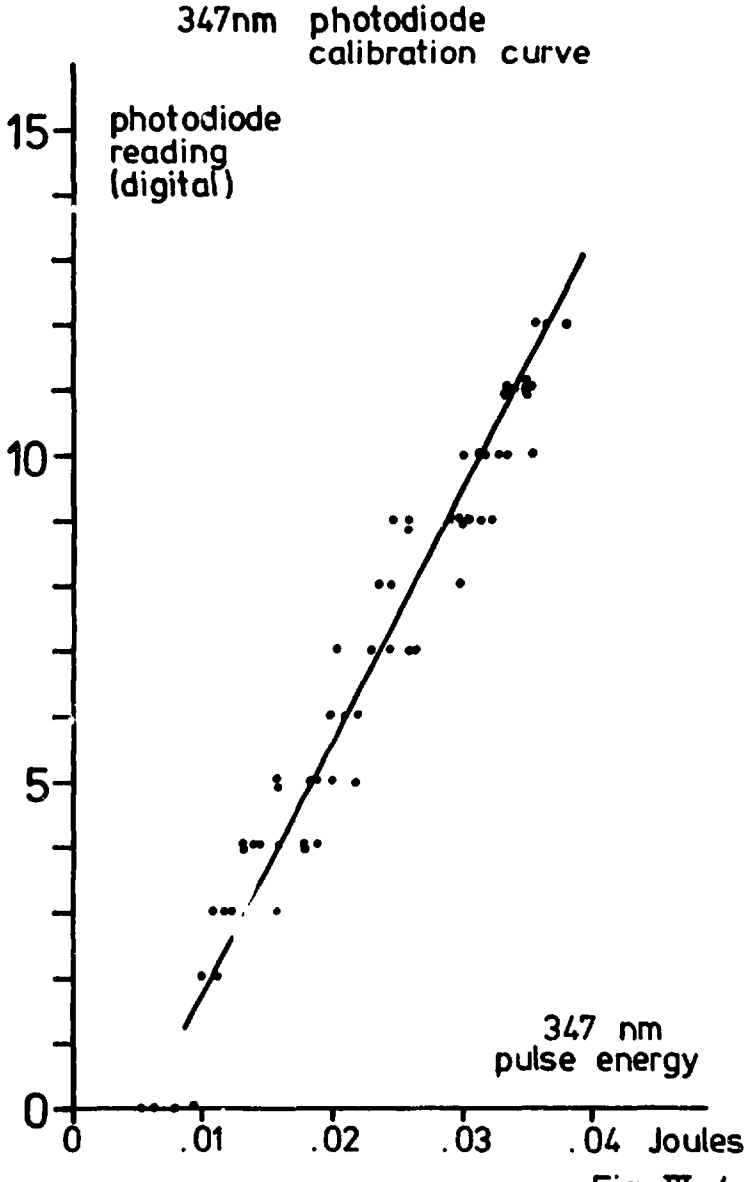

Fig. III. 4

Fig.III.5
June 26, 1975, 0845 CET
Scale factors see text!

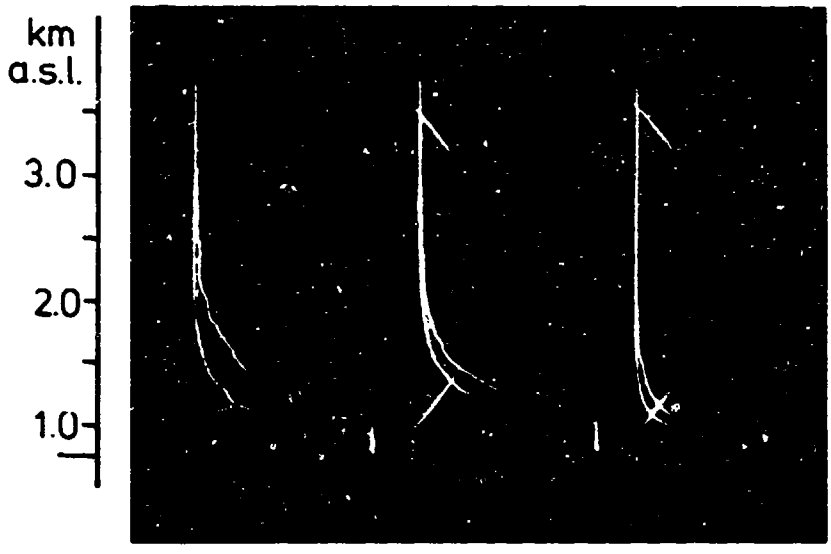

0930 CET 1103 CET 1155 CET

Fig.III.6
Aug. 23, 1974

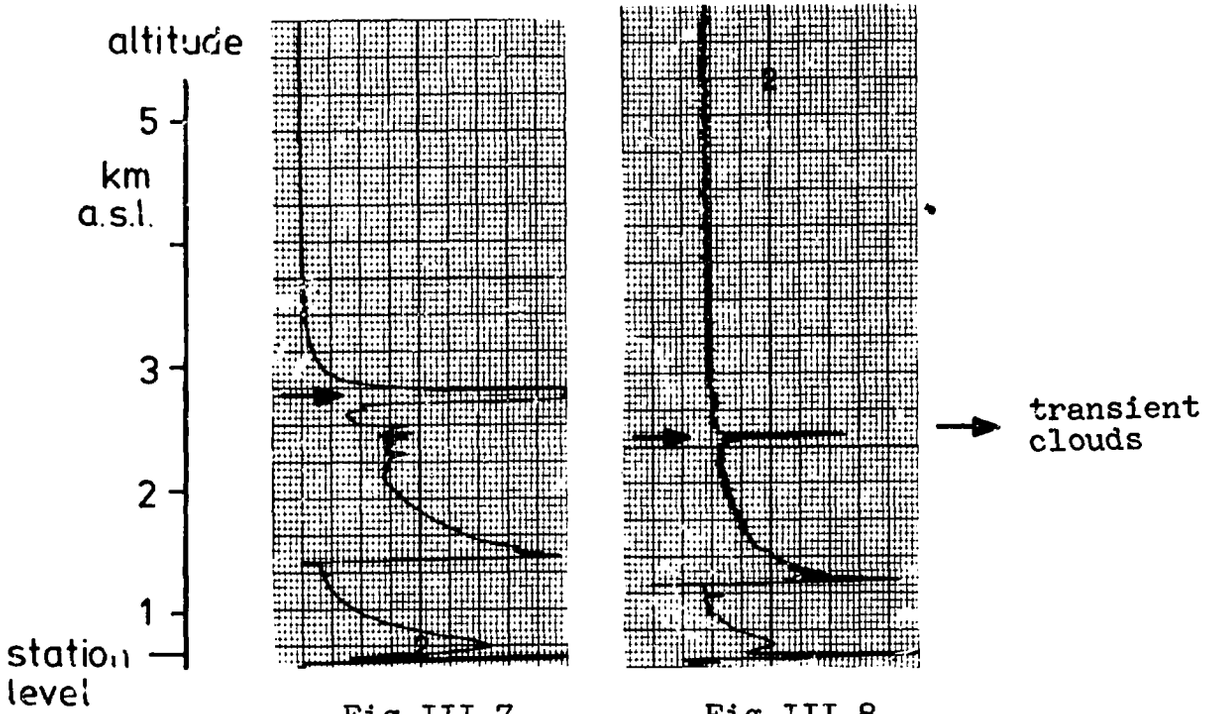

Fig.III.7 694 nm

Fig.III.8 347 nm

July 9, 1975, 1718 CET

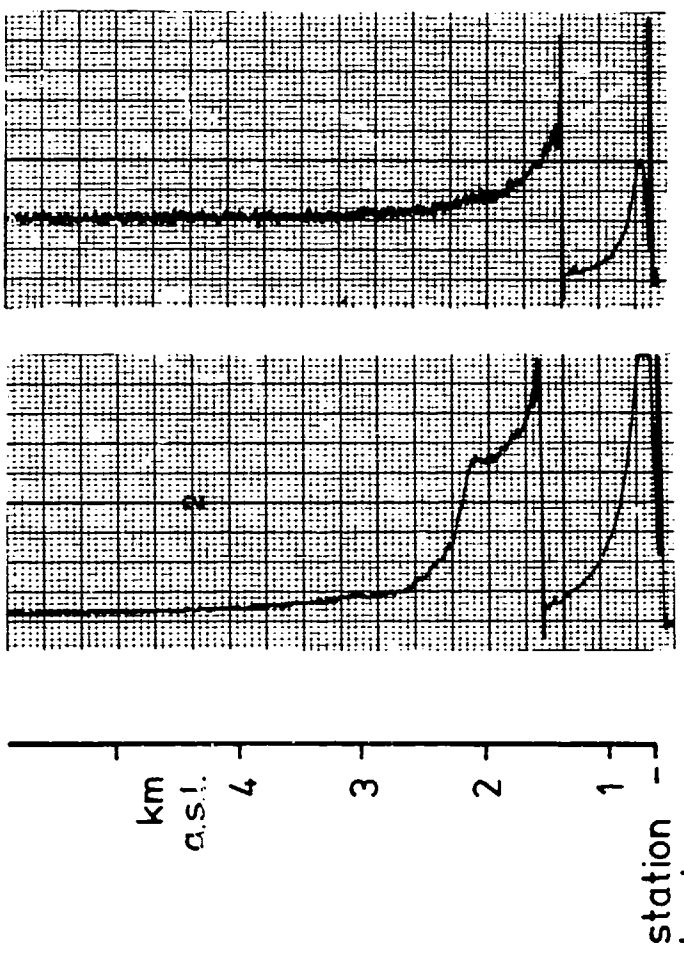

Fig.III.9
694 nm

Fig.III.10
347 nm

July 28, 1975, 1611 CET

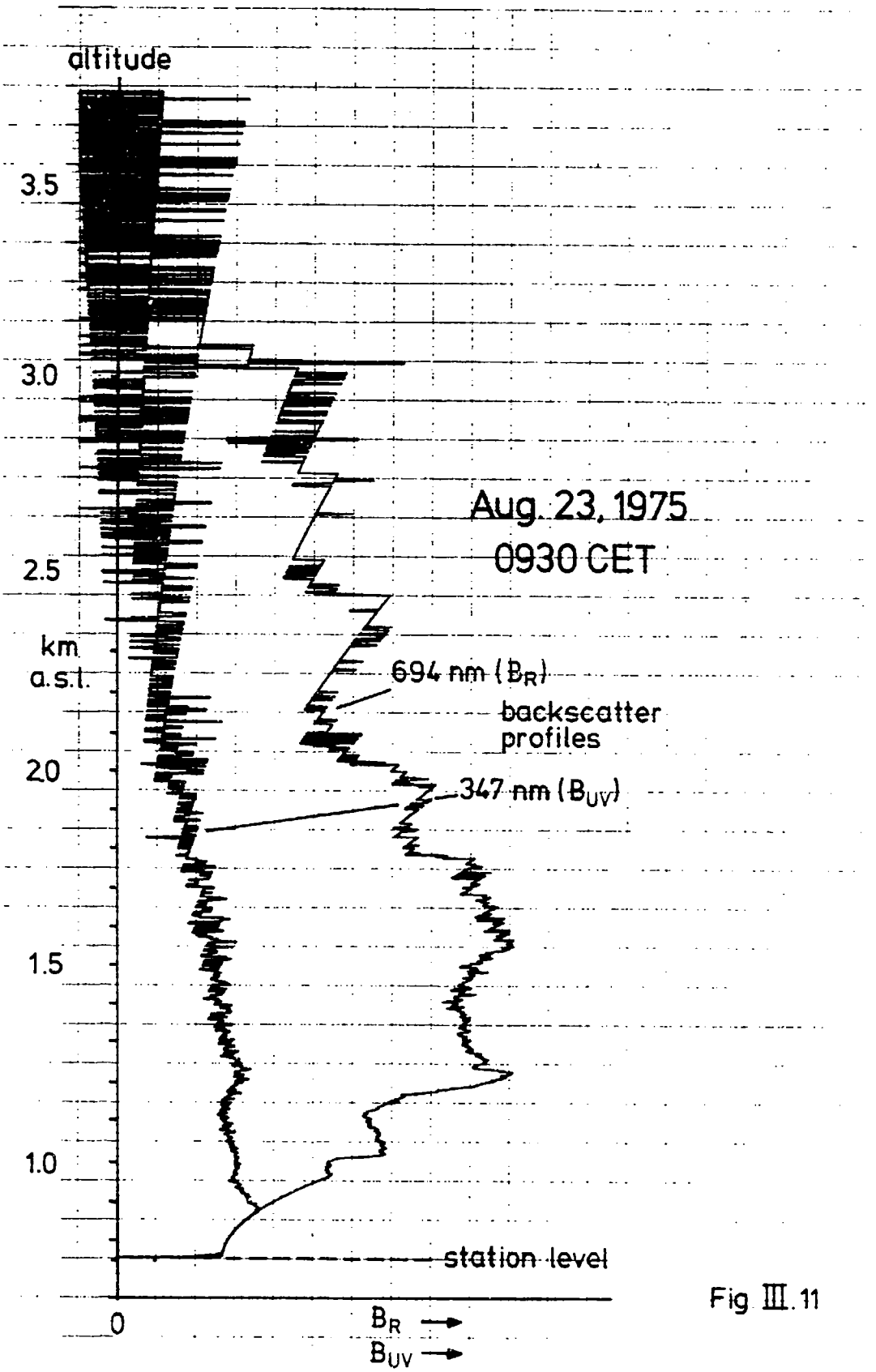
altitude
3.5
3.0
2.5
km
a.s.l.
2.0
1.5
1.0
Aug. 23, 1975
0930 CET
694 nm (B_R)
backscatter
profiles
347 nm (B_{UV})
station level
0
B_R
B_{UV}

Fig. III.11

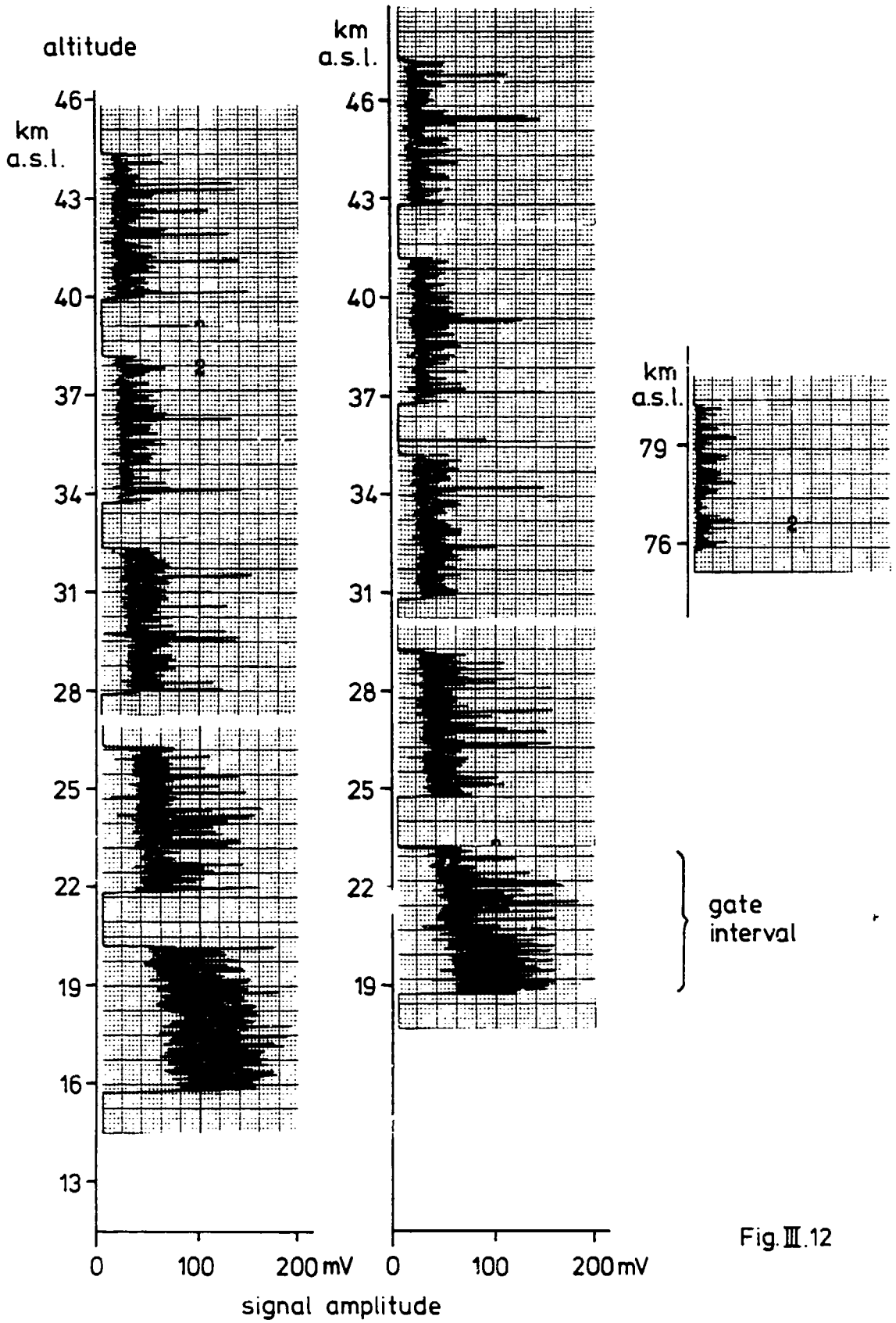
altitude
km
a.s.l.
46
43
40
37
34
31
28
25
22
19
16
13
km
a.s.l.
46
43
40
37
34
31
28
25
22
19
km
a.s.l.
79
76
gate
interval
0
100
200 mV
0
100
200 mV
signal amplitude

Fig. III.12

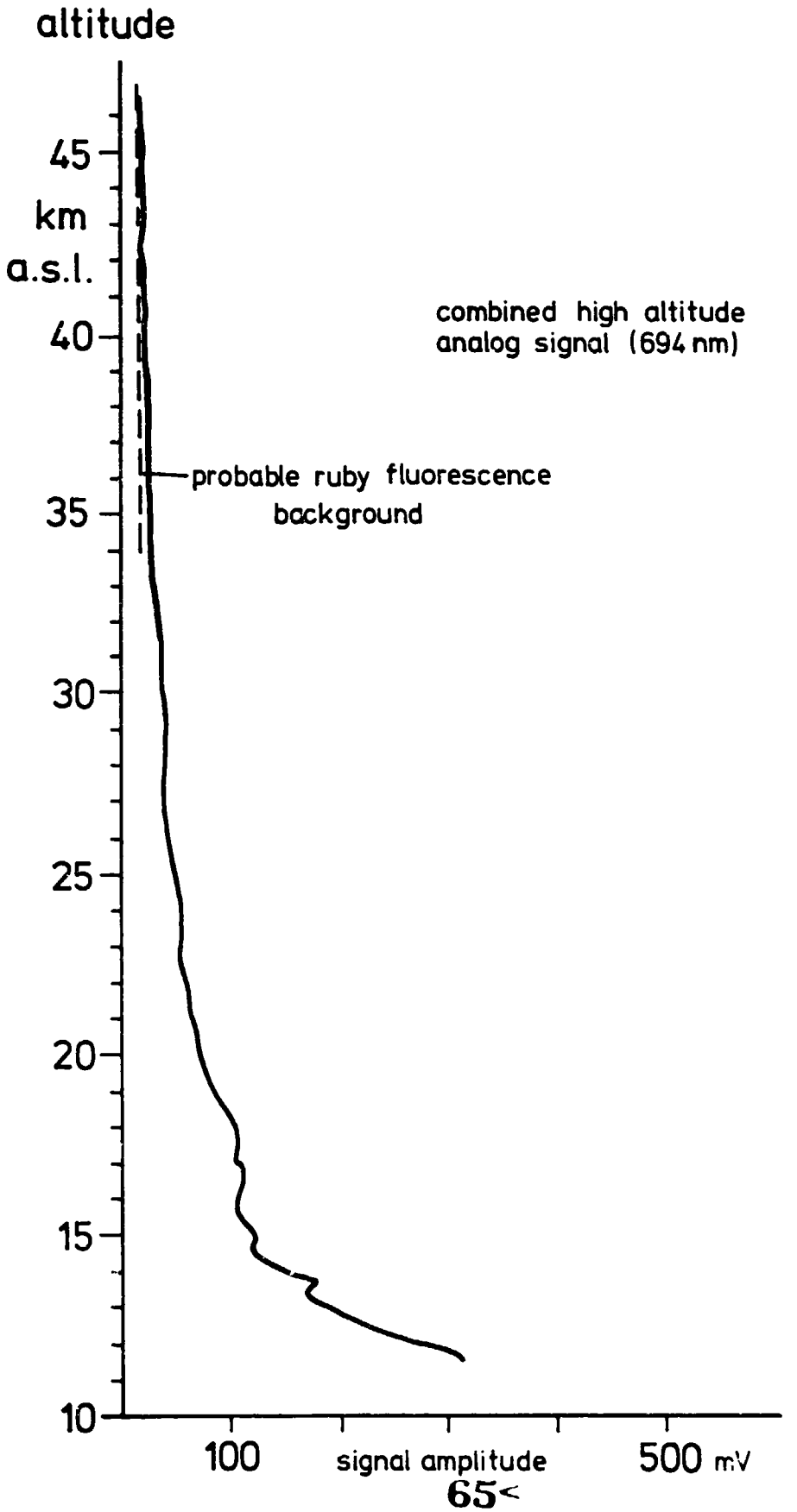
altitude
45
km
a.s.l.
40
35
30
25
20
15
10
combined high altitude
analog signal (694 nm)
probable ruby fluorescence
background
100
signal amplitude
500 mV

Fig. III.13

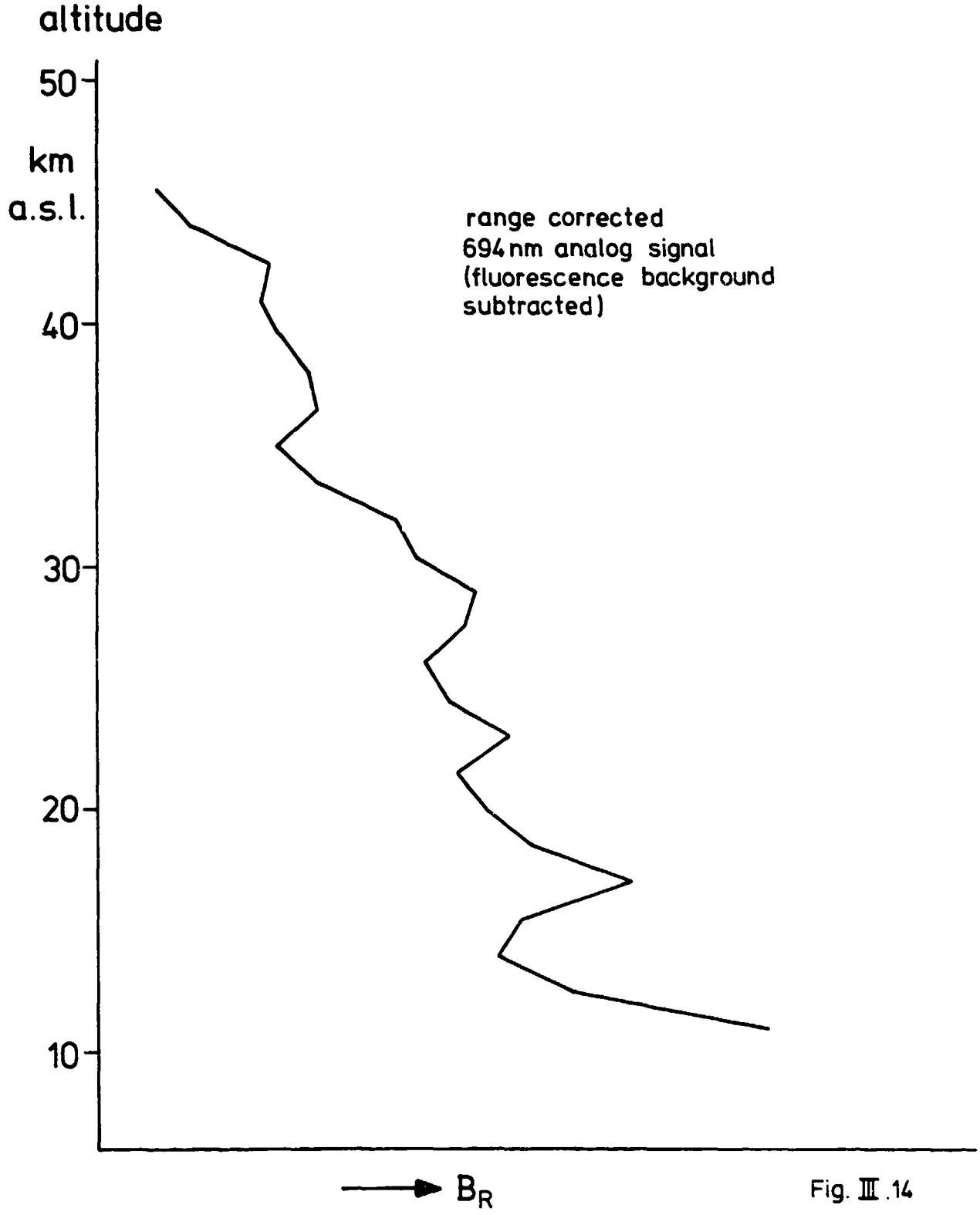
altitude
50
km
a.s.l.
40
30
20
10
range corrected
694 nm analog signal
(fluorescence background
subtracted)
B_R

Fig. III.14

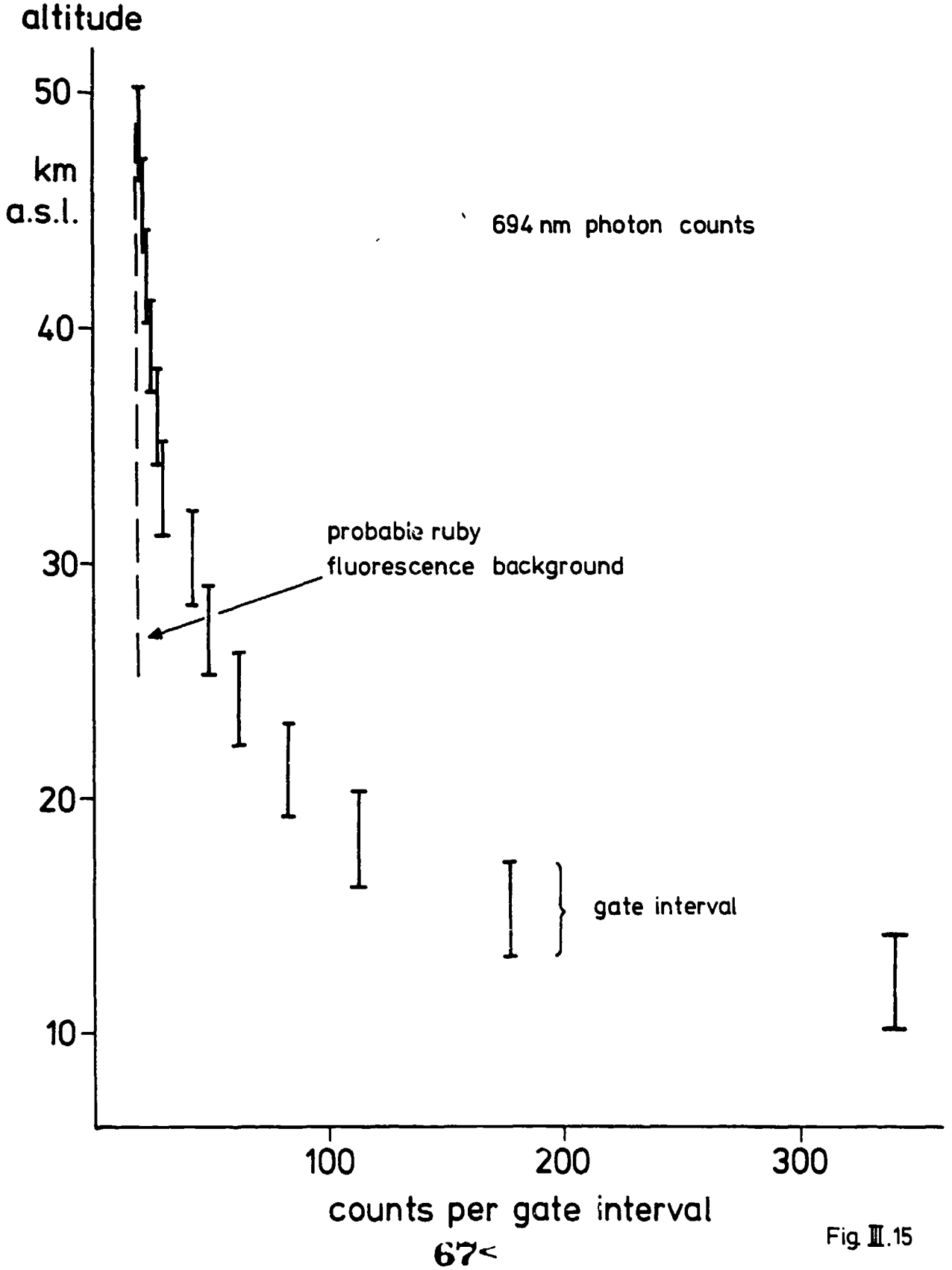
altitude
50
km
a.s.l.
40
30
20
10
694 nm photon counts
probable ruby
fluorescence background
gate interval
100
200
300
counts per gate interval

Fig. III.15

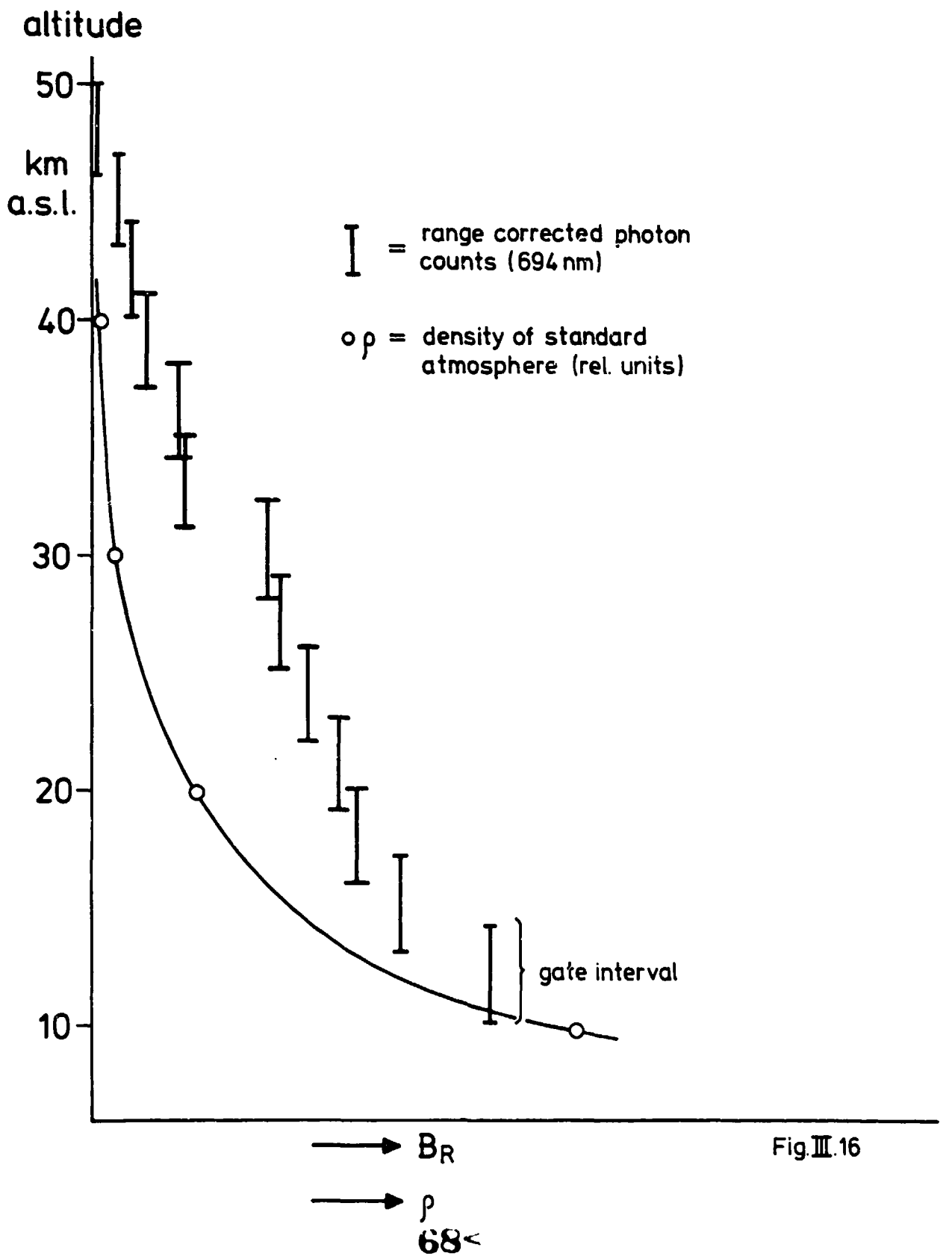
altitude
50
km
a.s.l.
40
30
20
10
= range corrected photon counts (694 nm)
o ρ = density of standard atmosphere (rel. units)
gate interval
B_R
ρ

Fig. III.16

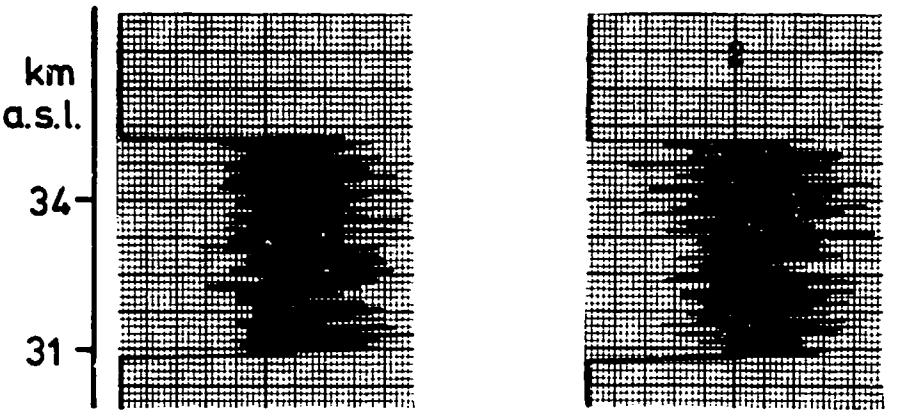

Fig.III.17
High altitude 694 nm analog signals without (left) and with (right) using the fluorescence suppression

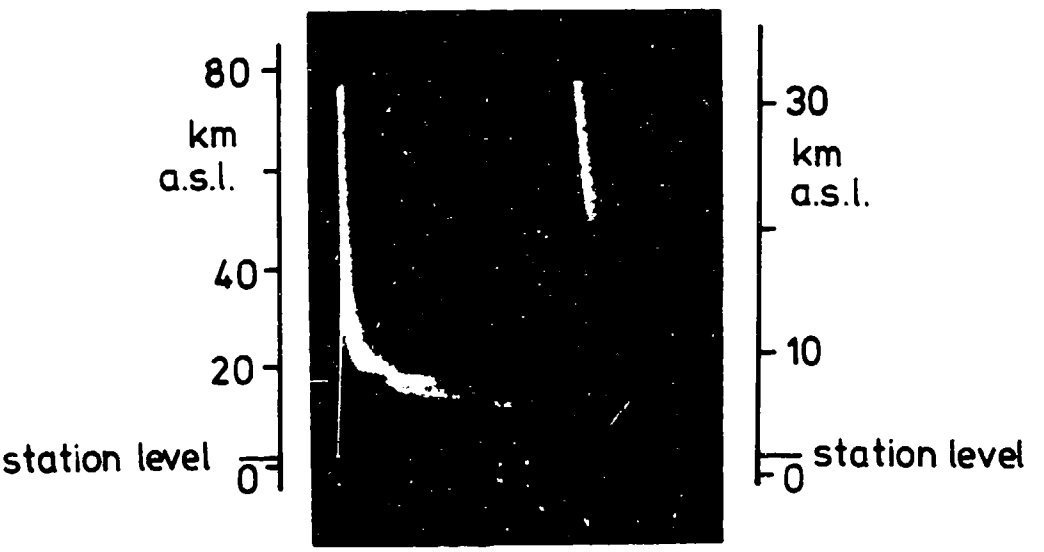

Fig.III.18
Jan. 10, 1975, 1900 CET
694 nm high altitude analog signals,
showing dust layer from Fuego volcano

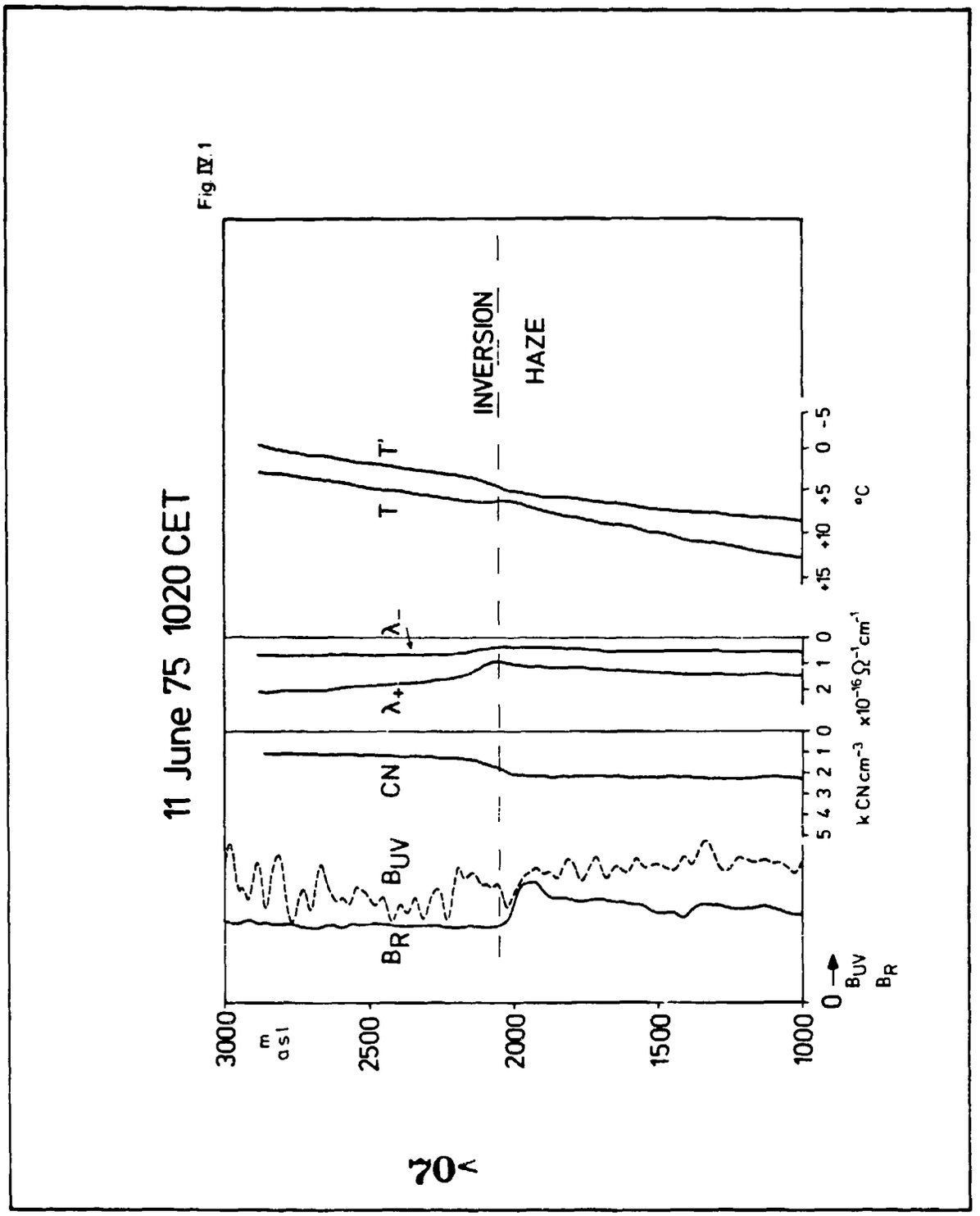
11 June 75 1020 CET
INVERSION
HAZE
T'
T
°C
λ-
λ+
CN
kCN cm⁻³
x10⁻¹⁶ Ω⁻¹cm⁻¹
B_UV
B_R
m asl
3000
2500
2000
1500
1000

Fig IV.1

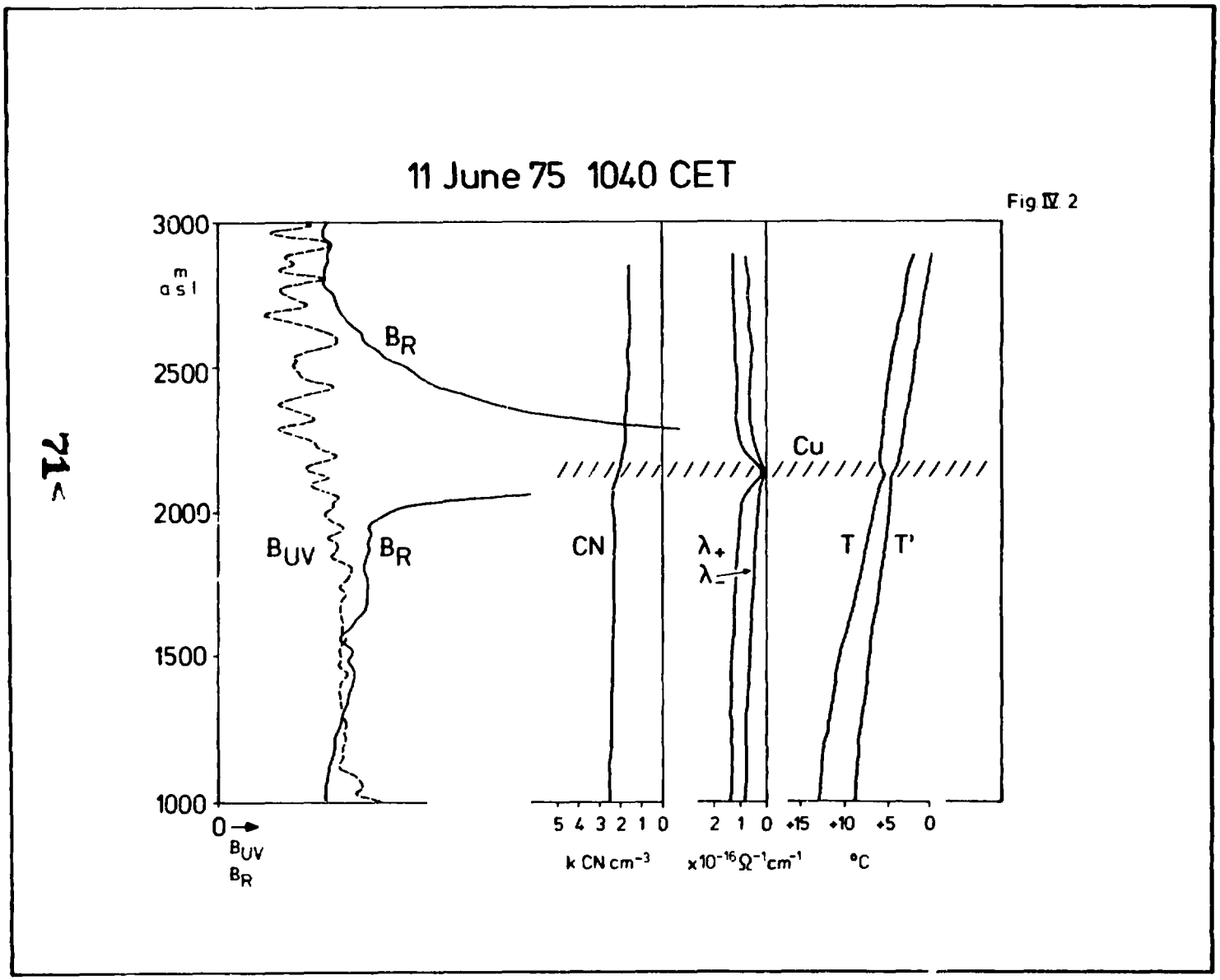
11 June 75 1040 CET
Fig IV. 2
3000
m
a s l
2500
2000
1500
1000
B_R
B_{UV}
B_R
Cu
CN
λ_+
λ_-
T
T'
0 →
B_{UV}
B_R
5 4 3 2 1 0
k CN cm^{-3}
2 1 0
x10$^{-16}\Omega^{-1}$cm^{-1}
+15 +10 +5 0
°C

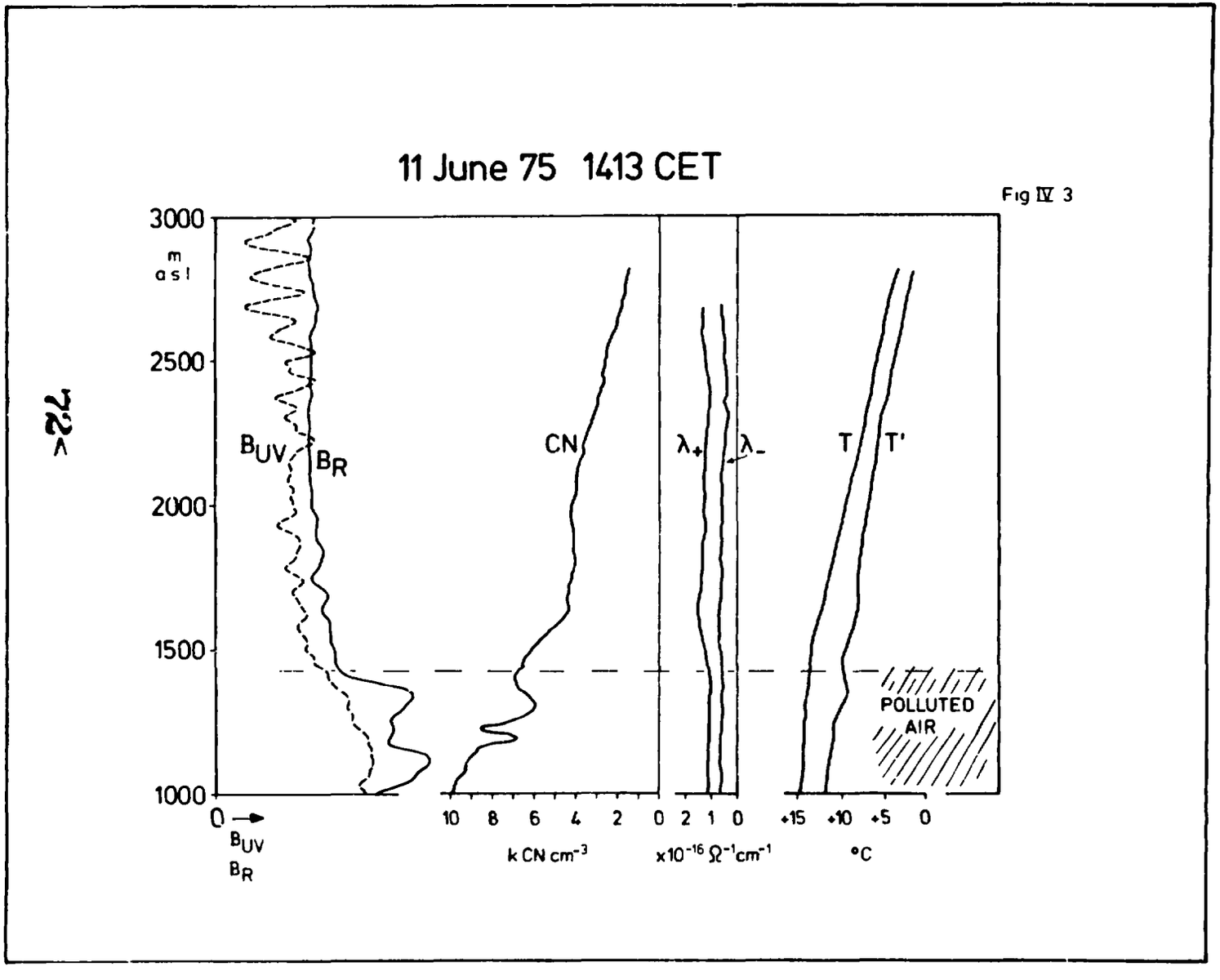
11 June 75 1413 CET
Fig IV 3
3000
m
a s l
2500
2000
1500
1000
B_{UV}
B_R
CN
λ_+
λ_-
T
T'
POLLUTED
AIR
0 →
B_{UV}
B_R
10 8 6 4 2 0
k CN cm^{-3}
0 2 1 0
x10^{-16} Ω^{-1}cm^{-1}
+15 +10 +5 0
°C

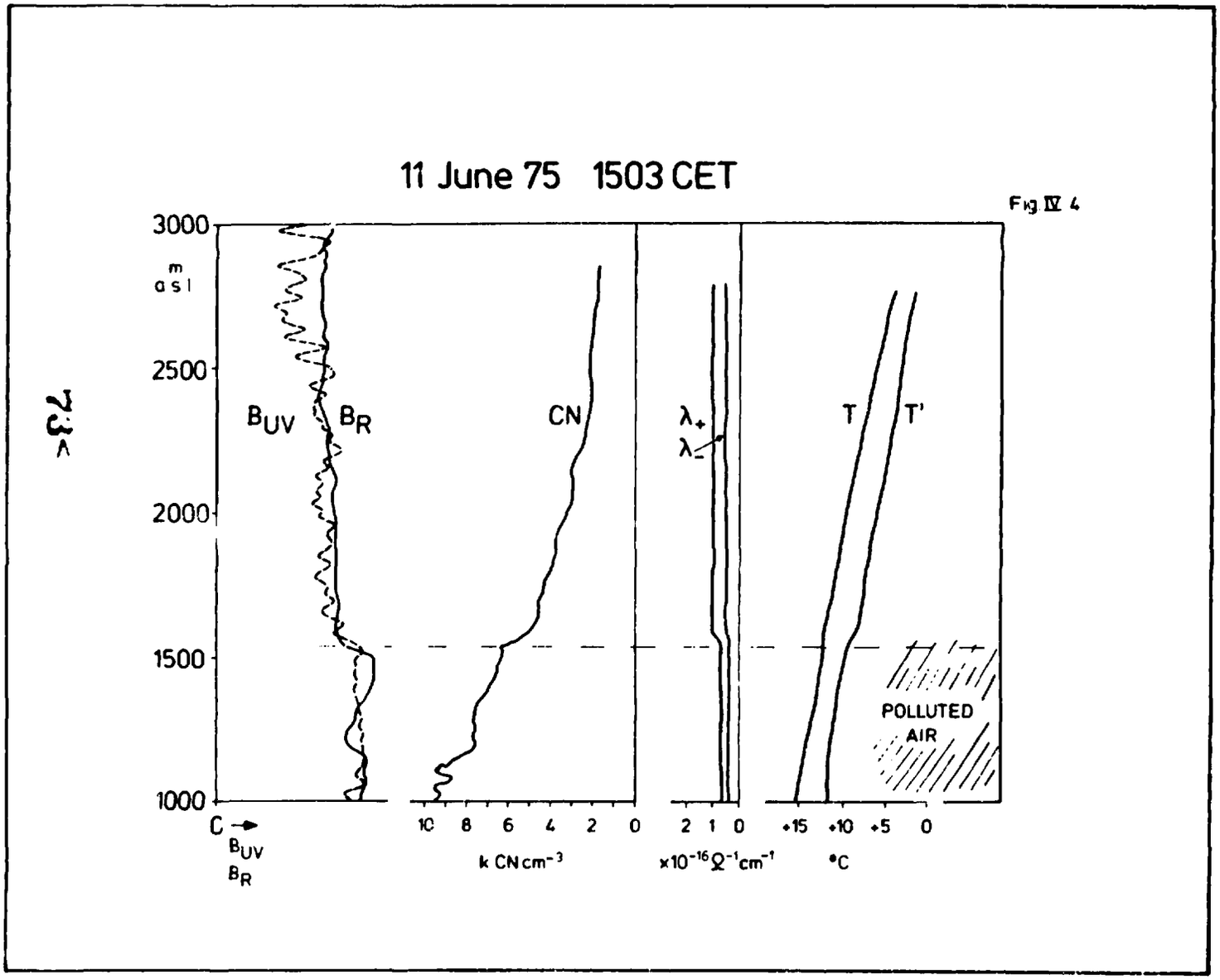
11 June 75 1503 CET
Fig. IV. 4
3000
m
a s l
2500
2000
1500
1000
B_{UV}
B_R
CN
λ_+
λ_-
T
T'
POLLUTED
AIR
C →
B_{UV}
B_R
10 8 6 4 2 0
k CN cm^{-3}
2 1 0
x10$^{-16}\Omega^{-1}$cm^{-1}
+15 +10 +5 0
°C

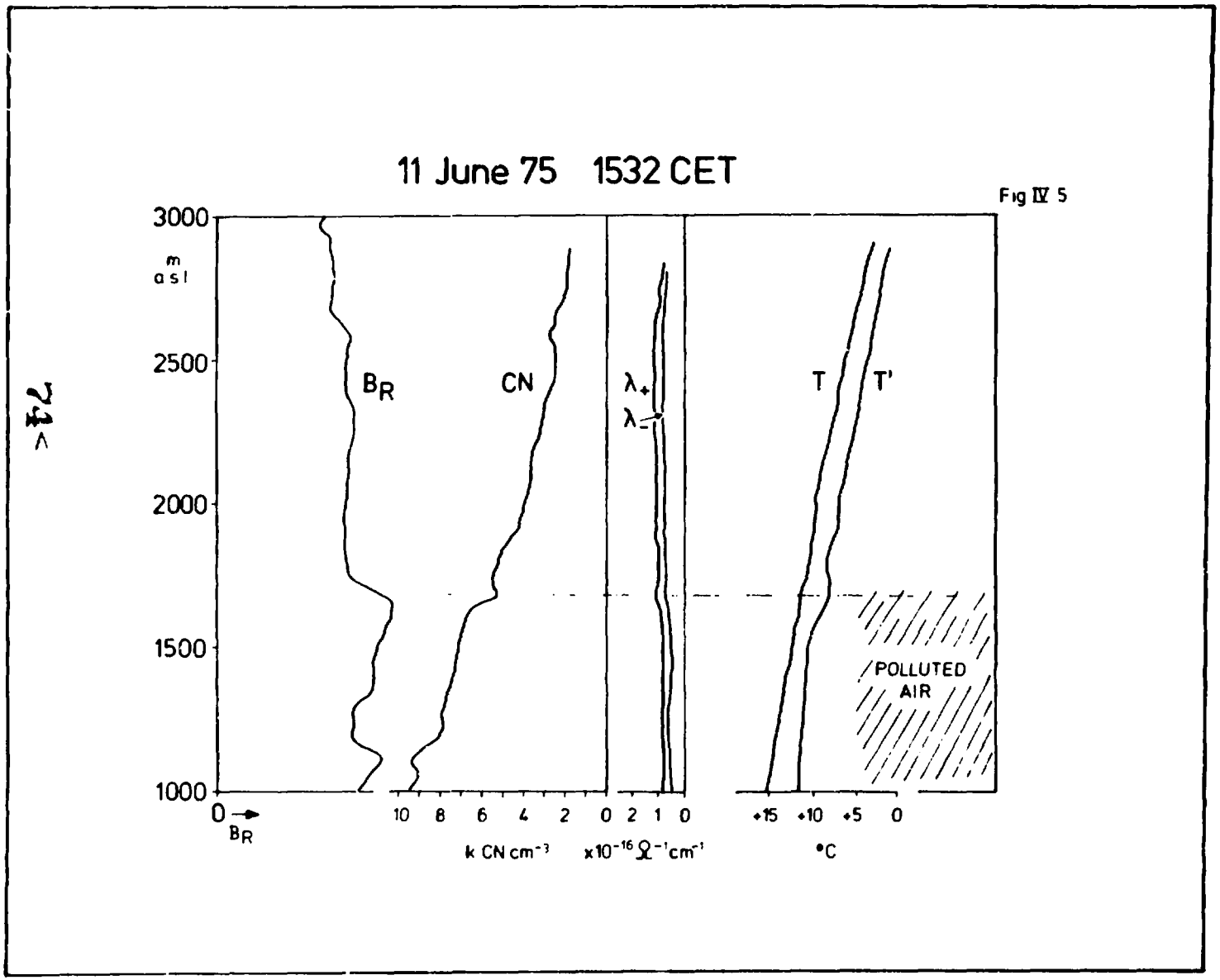
11 June 75 1532 CET
Fig IV 5
3000
m
a s l
2500
2000
1500
1000
B_R
CN
λ_+
λ_-
T
T'
POLLUTED
AIR
0 →
B_R
10 8 6 4 2 0
k CN cm^{-3}
2 1 0
x10^{-16} Ω^{-1}cm^{-1}
+15 +10 +5 0
°C

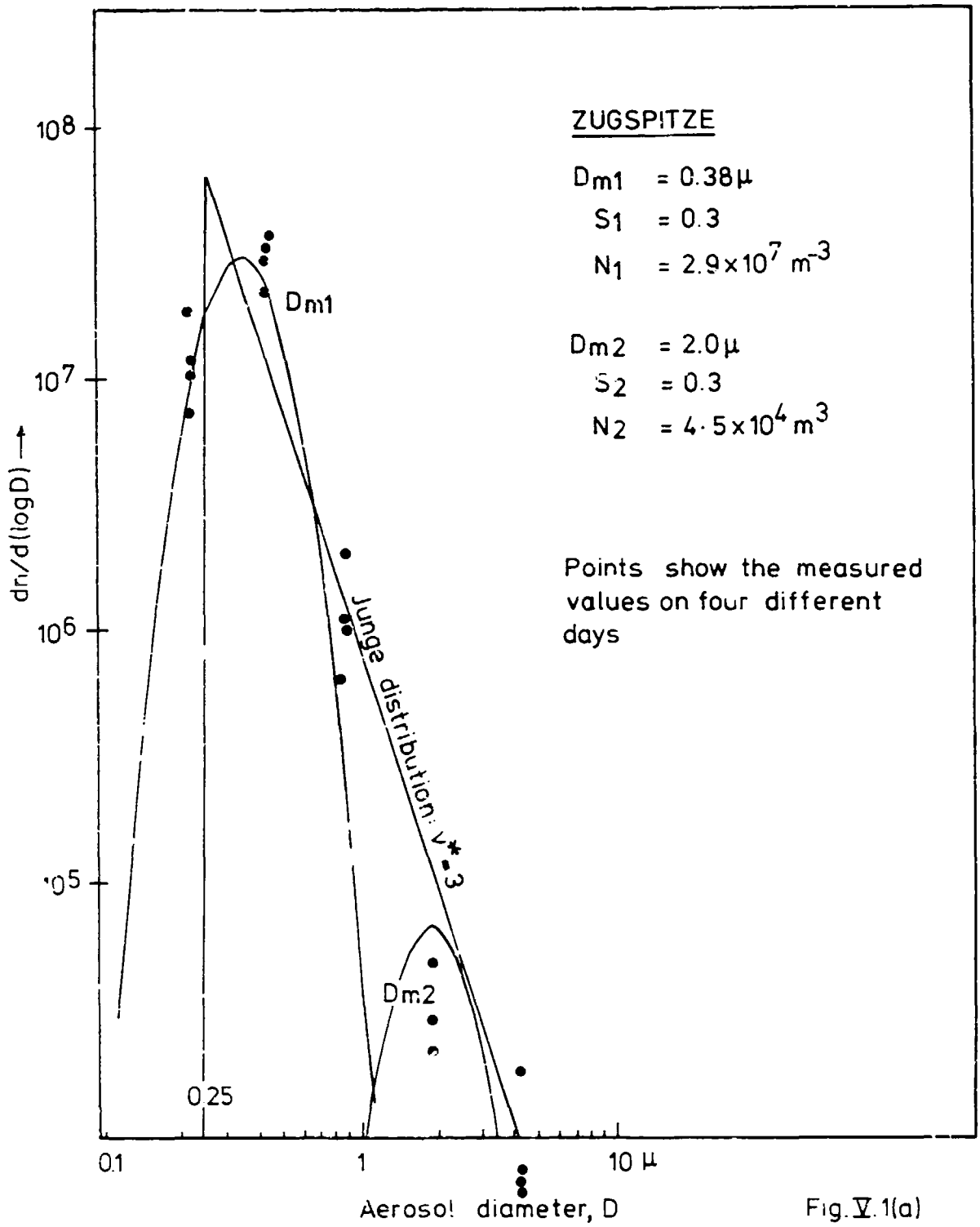
ZUGSPITZE
Dm1 = 0.38μ
S1 = 0.3
N1 = 2.9x10^7 m^-3
Dm2 = 2.0μ
S2 = 0.3
N2 = 4·5x10^4 m^3
Points show the measured values on four different days
Dm1
Dm2
Junge distribution: ν*=3
dn/d(logD)
10^8
10^7
10^6
10^5
0.25
0.1
1
10 μ
Aerosol diameter, D

Fig. V.1(a)

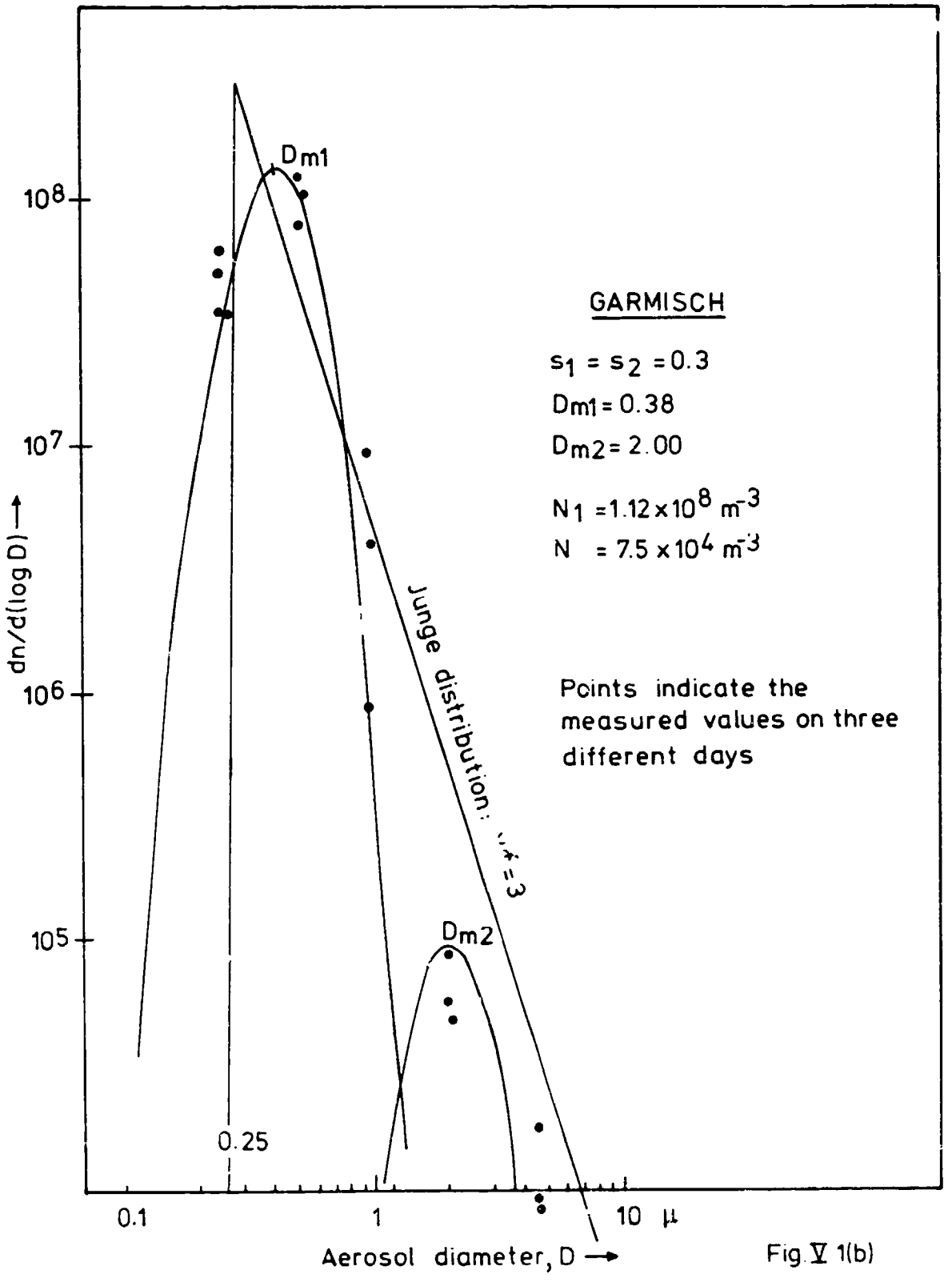
Dm1
10^8
10^7
10^6
10^5
dn/d(log D) →
GARMISCH
$s_1 = s_2 = 0.3$
$D_{m1} = 0.38$
$D_{m2} = 2.00$
$N_1 = 1.12 \times 10^8$ m^{-3}
$N = 7.5 \times 10^4$ m^{-3}
Junge distribution: ν = 3
Points indicate the measured values on three different days
Dm2
0.25
0.1
1
10 μ
Aerosol diameter, D →

Fig. V 1(b)

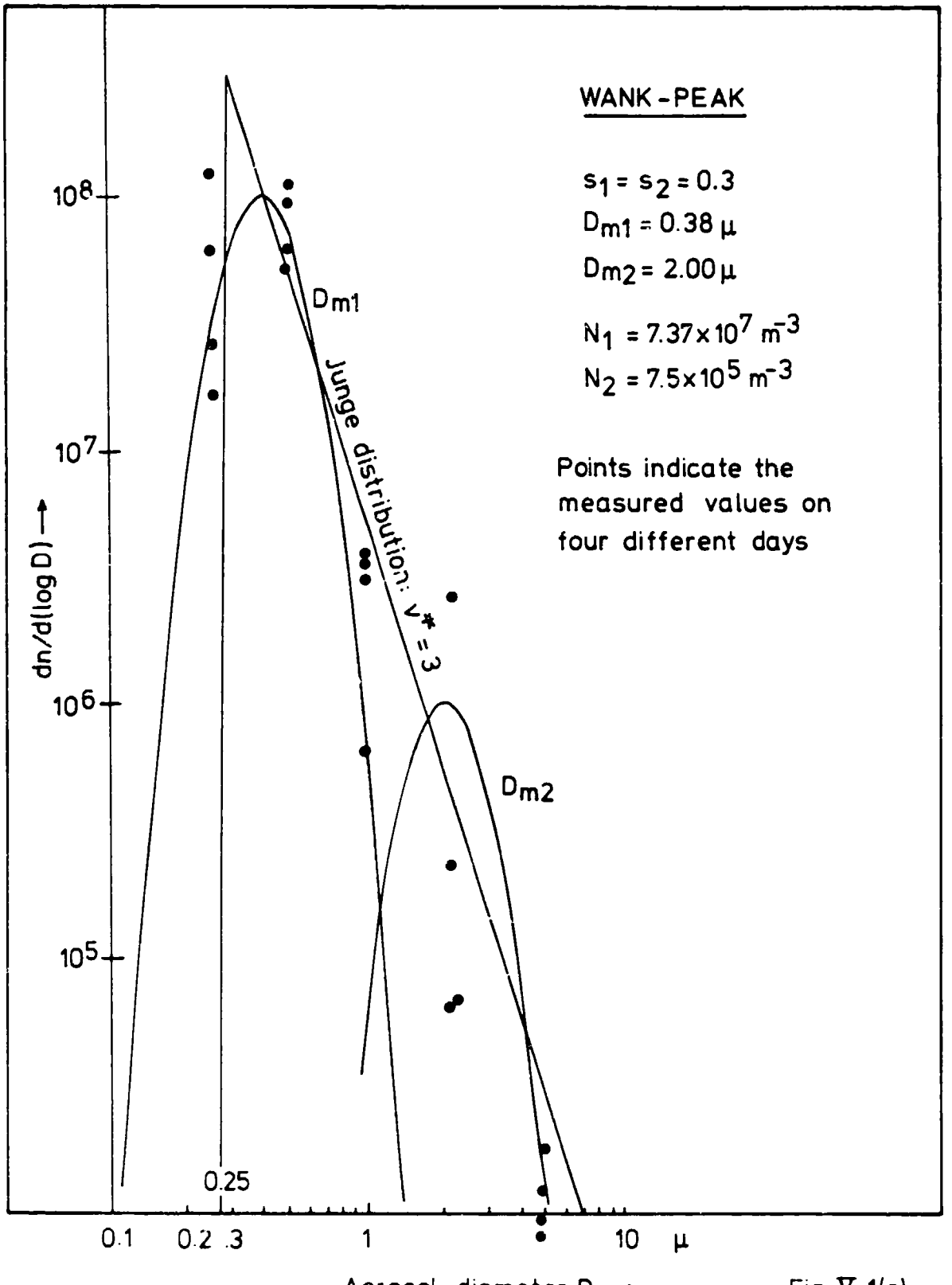
WANK - PEAK
$s_1 = s_2 = 0.3$
$D_{m1} = 0.38\,\mu$
$D_{m2} = 2.00\,\mu$
$N_1 = 7.37 \times 10^7\ m^{-3}$
$N_2 = 7.5 \times 10^5\ m^{-3}$
Points indicate the measured values on four different days
10^8
10^7
10^6
10^5
dn/d(log D) →
D_{m1}
Junge distribution: $\nu^* = 3$
D_{m2}
0.25
0.1
0.2
.3
1
10
μ
Aerosol diameter, D →

Fig. V.1(c)

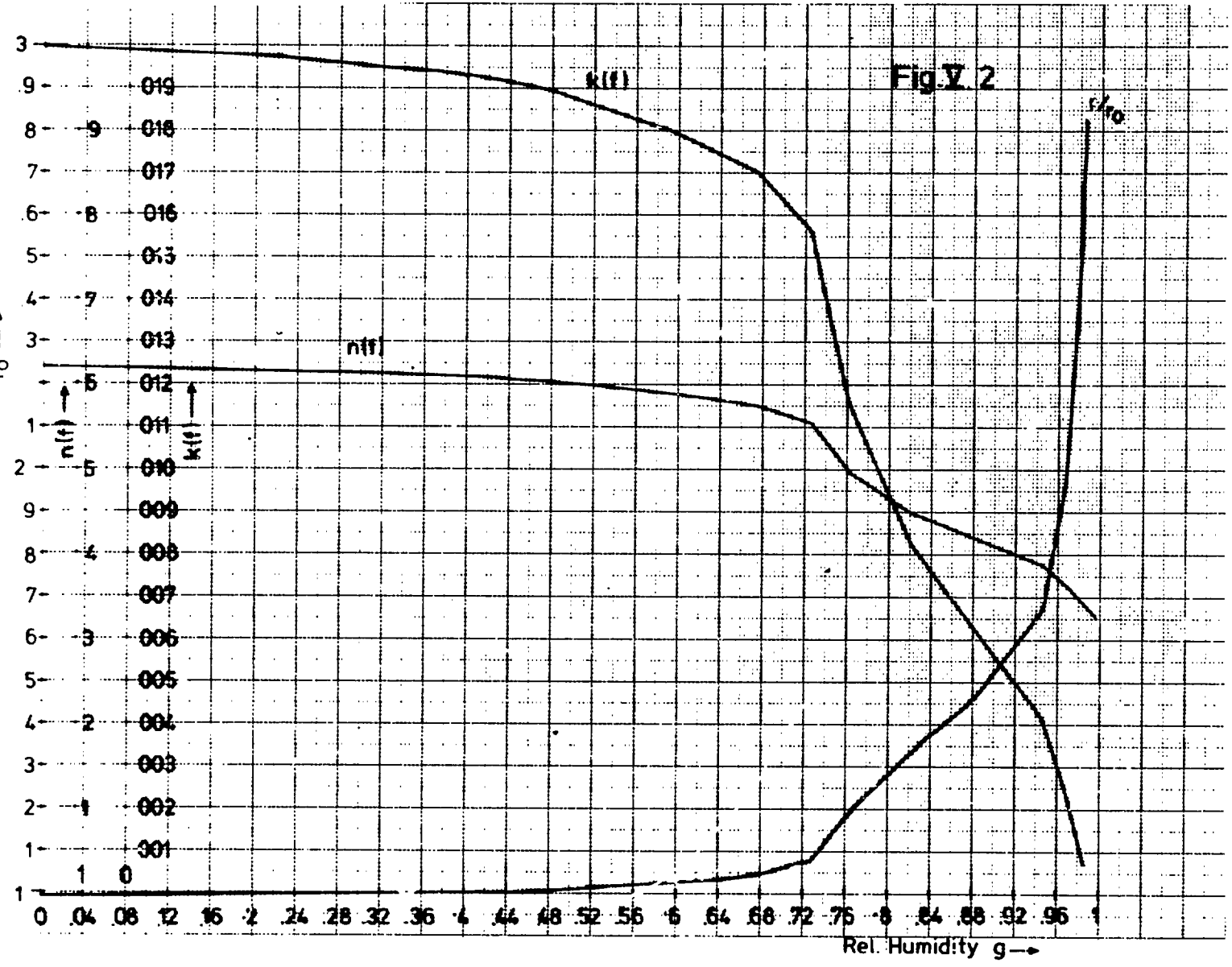
k(f)
n(f)
r/r0
n(f) →
k(f) →
r/r0 →
Rel. Humidity g →
0 .04 .08 .12 .16 .2 .24 .28 .32 .36 .4 .44 .48 .52 .56 .6 .64 .68 .72 .76 .8 .84 .88 .92 .96 1
1 0
3 9 8 7 6 5 4 3 2 1 9 8 7 6 5 4 3 2 1
019 018 017 016 015 014 013 012 011 010 009 008 007 006 005 004 003 002 001
9 8 7 6 5 4 3 2 1 0

Fig.V. 2

CALIBRATED DOUBLE FREQUENCY LID

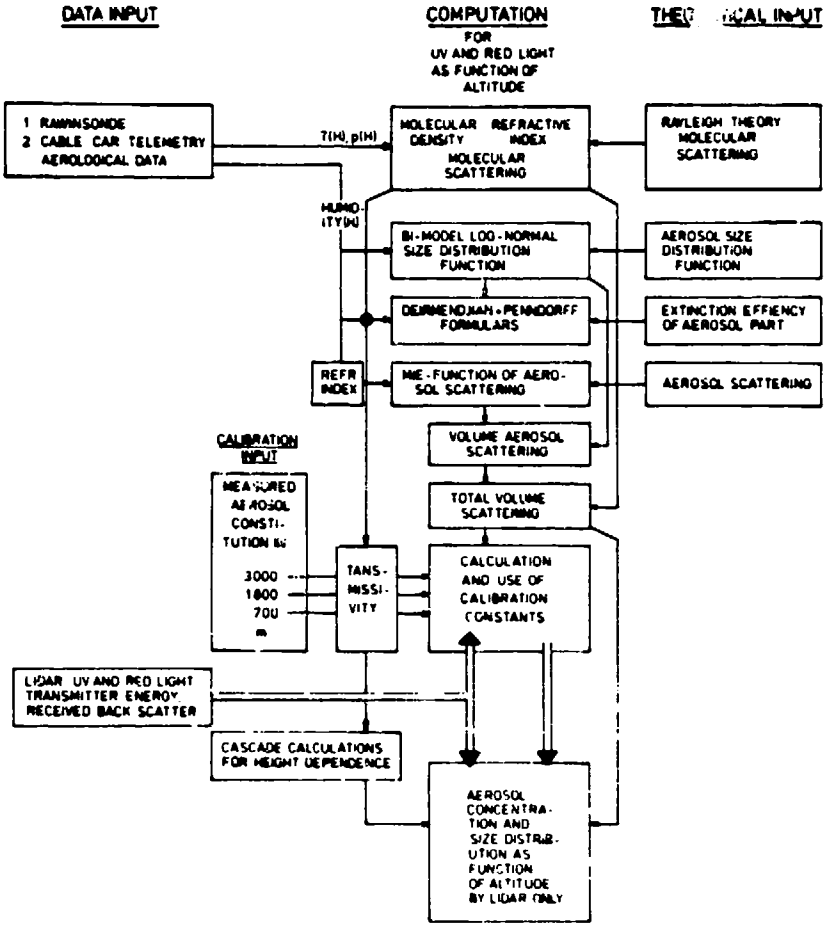

Fig.V.5

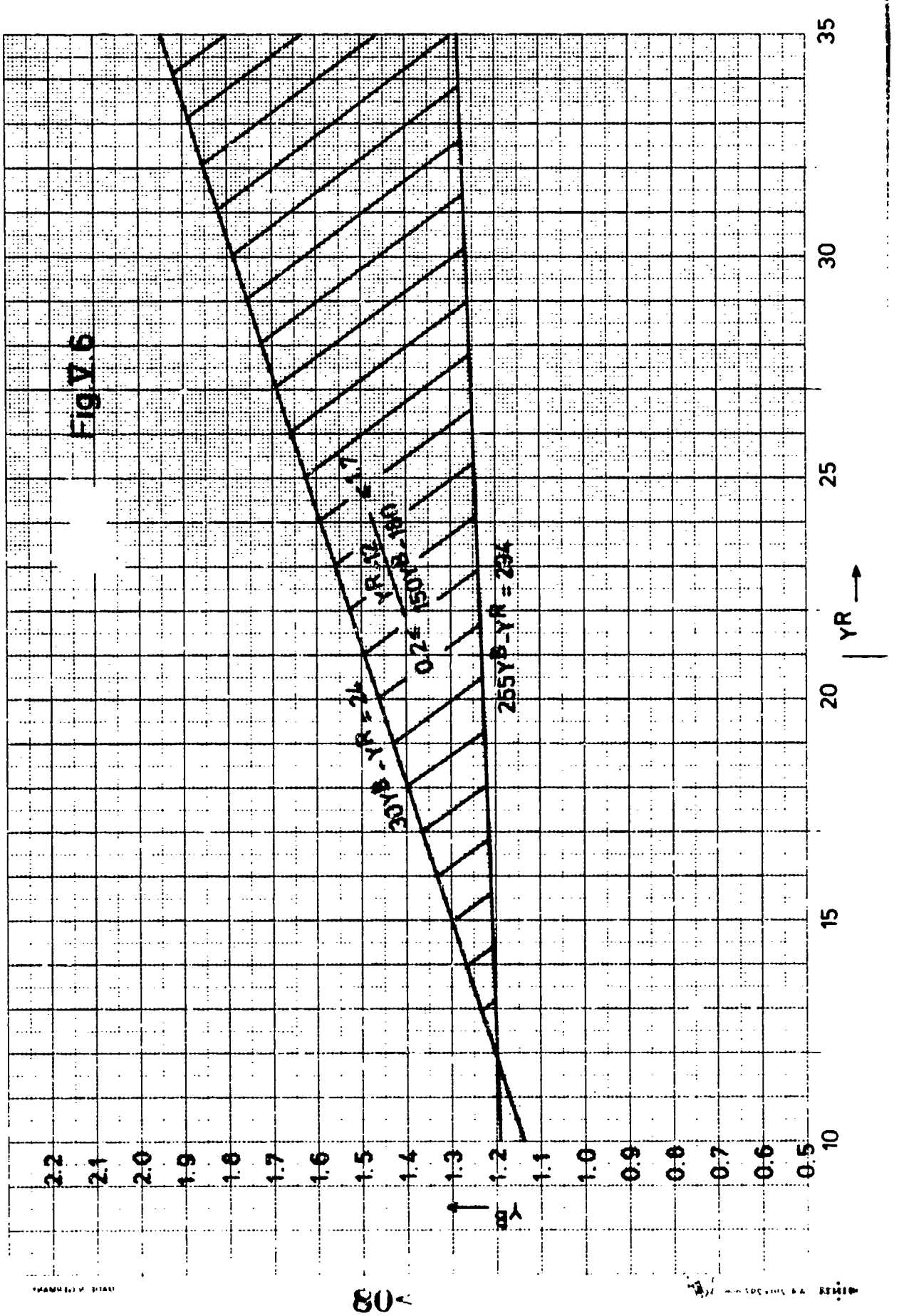
Fig V.6
35
30
25
20
15
10
YR
2.2
2.1
2.0
1.9
1.8
1.7
1.6
1.5
1.4
1.3
1.2
1.1
1.0
0.9
0.8
0.7
0.6
0.5
γm
255Y^B-Y^R = 294
0.2≠ 150Y^B-Y^R
30Y^B-Y^R=2≠
≠1

Fig. VII.1

Iterative computation of aersol density profiles

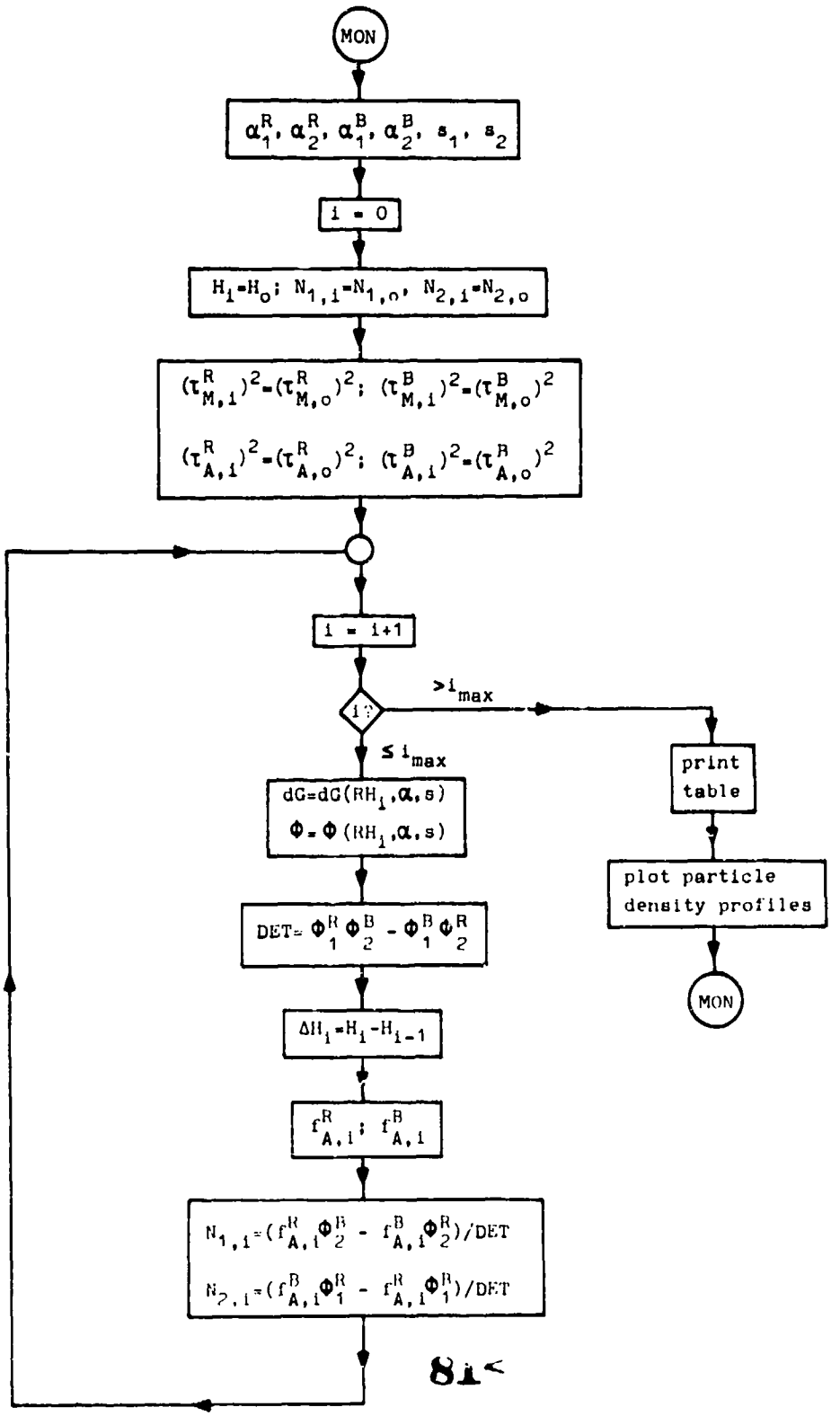

Fig.VII.2

Lidar backscatter intensity normalization and distance square correction

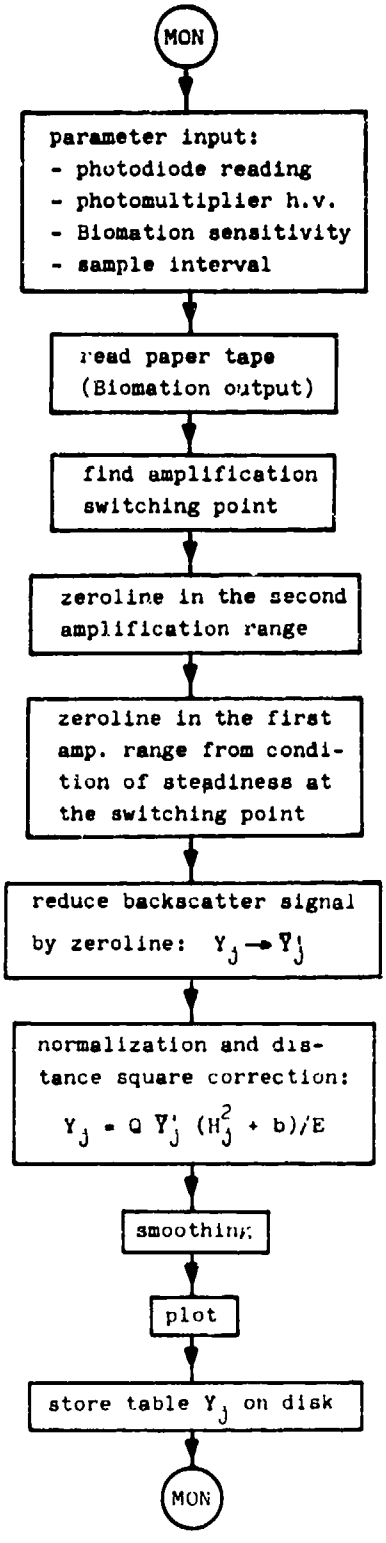

Combining lidar data with radiosonde soundings

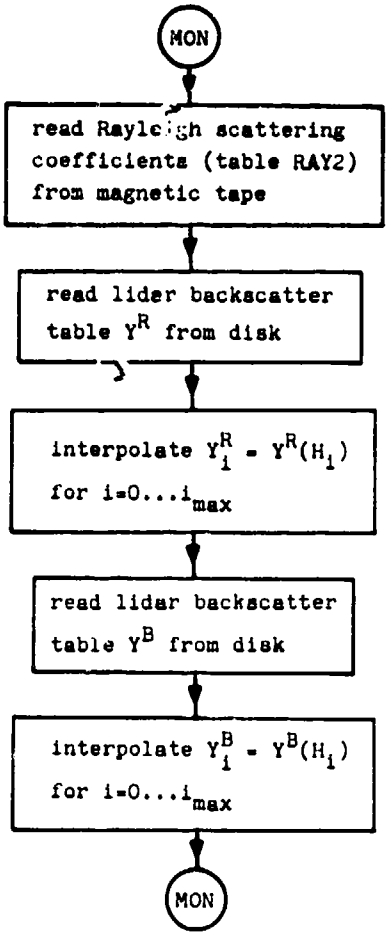

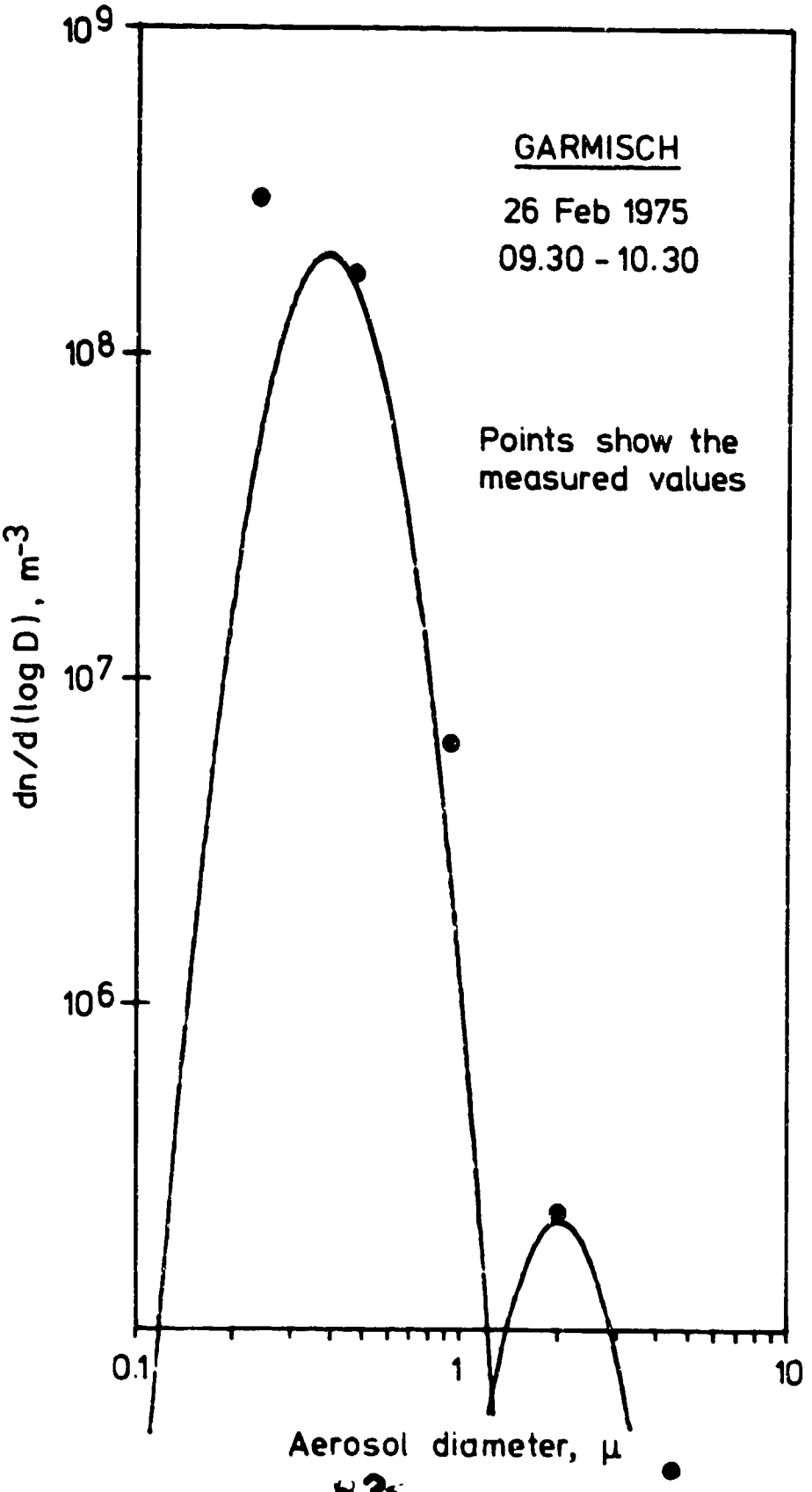
GARMISCH
26 Feb 1975
09.30 - 10.30
Points show the measured values
10^9
10^8
10^7
10^6
dn/d(log D), m^{-3}
0.1
1
10
Aerosol diameter, μ

Fig VII. 3a

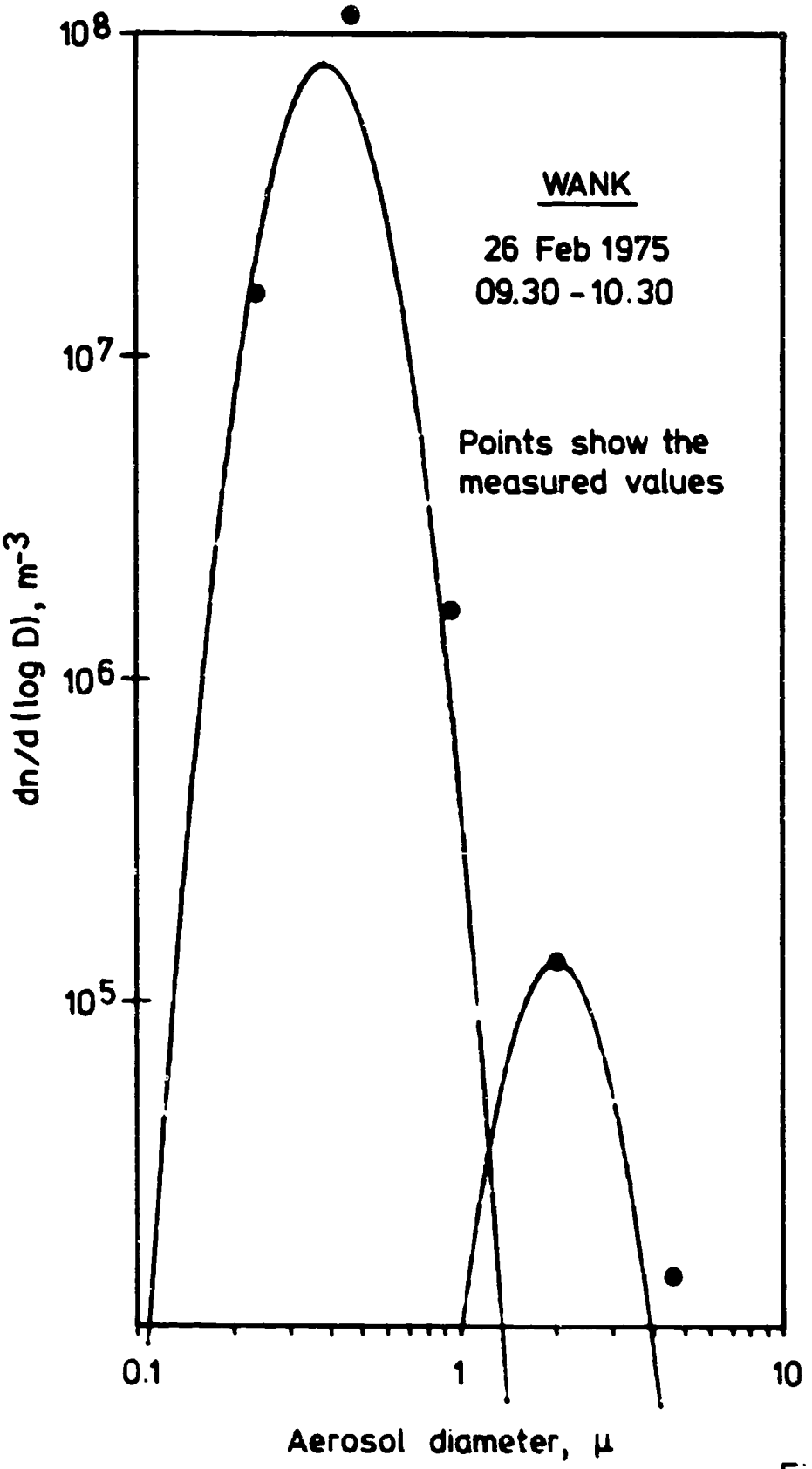
WANK
26 Feb 1975
09.30 - 10.30
Points show the measured values
dn/d (log D), m-3
10^8
10^7
10^6
10^5
0.1
1
10
Aerosol diameter, μ

Fig. VII. 3b

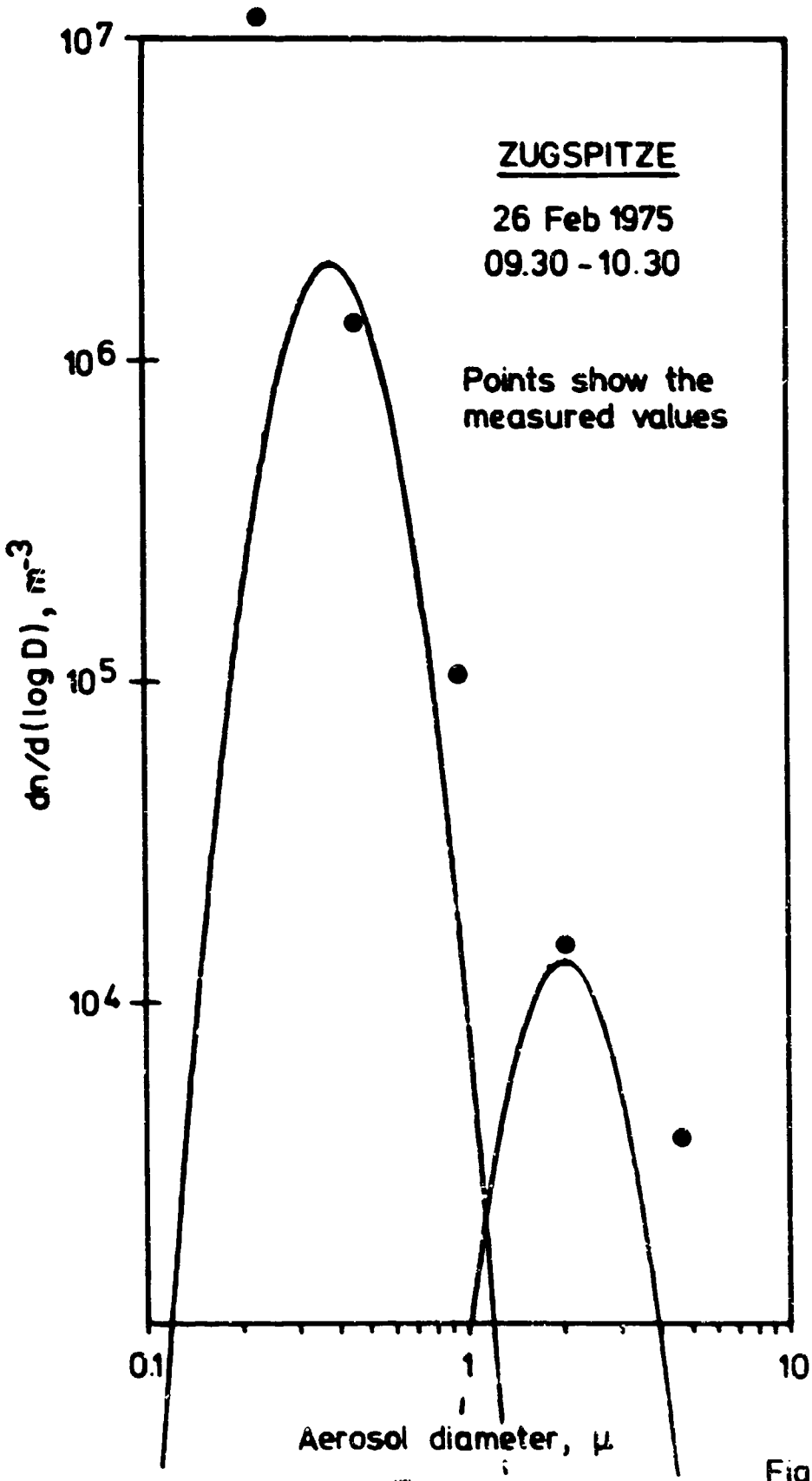
ZUGSPITZE
26 Feb 1975
09.30 - 10.30
Points show the measured values
10^7
10^6
10^5
10^4
dn/d(log D), m^{-3}
0.1
1
10
Aerosol diameter, μ

Fig. VI. 3c

Fig VII 4

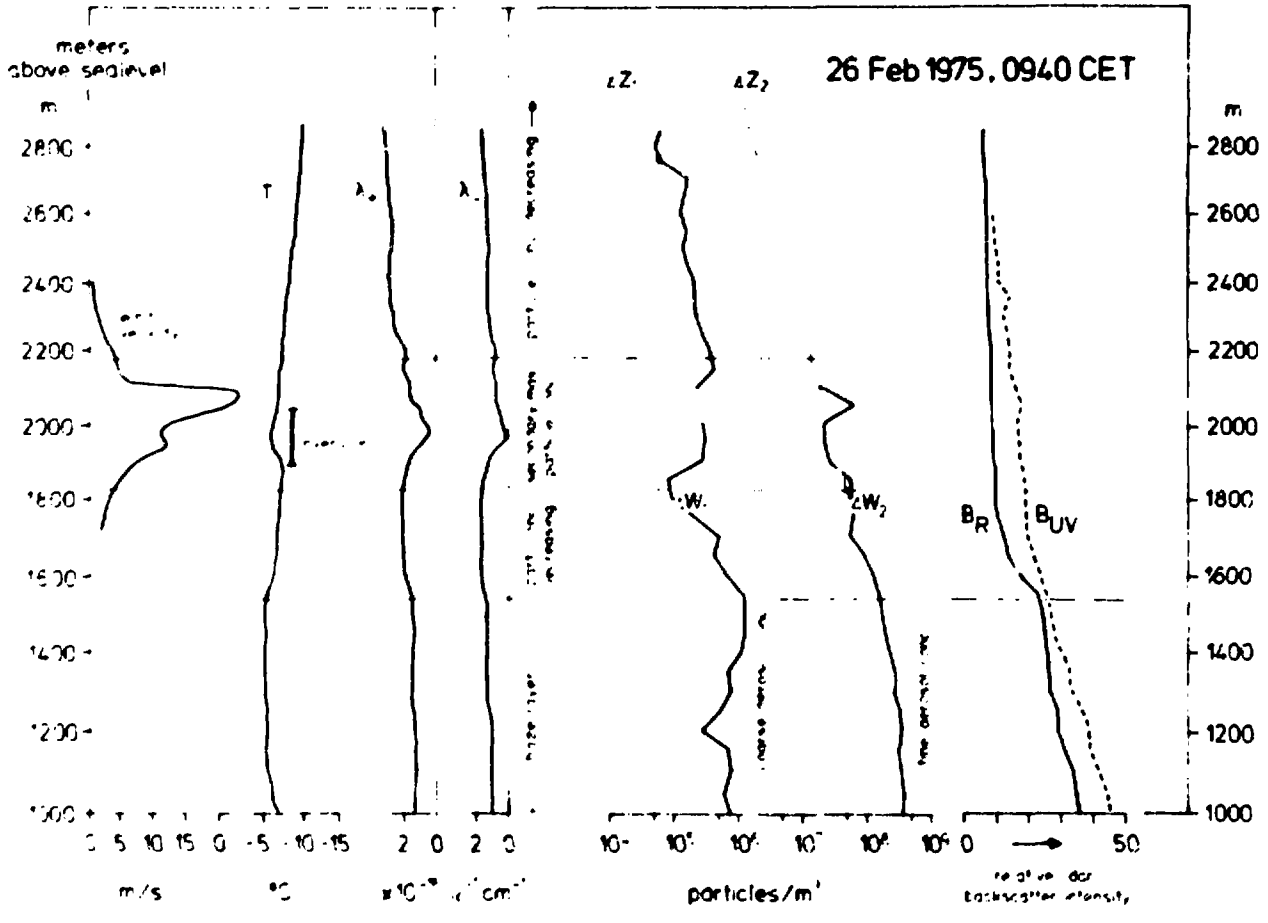
meters
above sealevel
m
26 Feb 1975, 0940 CET
T
λ_s
λ_r
ΔZ_1
ΔZ_2
W_1
W_2
B_R
B_{UV}
2800
2600
2400
2200
2000
1800
1600
1400
1200
1000
0 5 10 15 0 -5 -10 -15
2 0 2 0
10^{-} 10^{1} 10^{2} 10^{3} 10^{4} 10^{5}
0 50
m/s
°C
particles/m³